A Neural Network-Based Modeling and Prediction of Crater Formation and Evolution in Plume-Surface Interaction

by

Srijan Satyal

A thesis submitted to the Graduate Faculty of
Auburn University
in partial fulfillment of the
requirements for the Degree of
Master of Science

Auburn, Alabama
May 2, 2026

Keywords: Plume–Surface Interaction, Plume-Induced Cratering, Convolutional Neural Network, Crater Evolution Modeling, Polynomial feature map

Approved by

Nek Sharan, Chair, Assistant Professor of Aerospace Engineering
Brian Thurow, Professor of Aerospace Engineering
Vrishank Raghav, Associate Professor of Aerospace Engineering

Abstract

Retro-propulsive landings on extraterrestrial surfaces pose significant risks due to the interaction between the supersonic plume from rocket nozzles and the ground. The plume–surface interaction (PSI) releases dust and gravel, creating uncertainties in landing safety, spacecraft integrity, and environmental impact. To improve the understanding of PSI, the Physics Focused Ground Test (PFGT) campaign was conducted at NASA Marshall, generating high-quality PSI data on impingement pressures, plume flow structures, crater evolution, and ejecta dynamics under various nozzle heights, mass flow rates, ambient pressures, and regolith simulants. The crater geometries and their transitions reflect underlying erosion mechanisms such as viscous erosion, bearing capacity failure, and diffusion-driven shearing, which remain poorly understood under different flow and soil conditions.

This thesis aims to develop a predictive model for crater evolution by extracting and classifying crater geometries from PFGT high-speed experimental videos. Firstly, two different Convolutional Neural Networks (CNNs), edge-based and segmentation-based, were trained to automate crater edge extraction and region segmentation. The segmentation-based network outperformed the edge-based network, accurately identifying crater profiles across most experimental conditions. Secondly, another CNN, trained on manually labeled data, was employed to automate crater shape classification, which included parabolic, annular, conical-parabolic, conical-annular, and conical-deep categories, with high accuracy, thereby enabling the automated detection and analysis of crater shape transitions.

Finally, a data-driven parametric model is investigated using polynomial functions to model crater volume evolution under various operating conditions. Polynomial feature maps are employed to model crater volume evolution. Single-parameter coefficient models are used to model crater-volume evolution when only one operating parameter is varied. They provide

a robust framework for modeling parameter-dependent temporal evolution; however, the limited experimental data restricted the predictive accuracy of the model, especially in transitional regimes.

Artificial Intelligence (AI) Use Disclosure Statement

In the preparation of this thesis, the following Artificial Intelligence (AI) tools were used: ChatGPT, Grammarly, and Writefull. These tools were used primarily to check grammar and refine sentence structure and language of this thesis. The author acknowledges full responsibility for the intellectual content of this work and has ensured that all AI-assisted sections have been reviewed and revised for accuracy and appropriate academic style. All AI-generated content was reviewed and validated for relevance, appropriateness, and accuracy before incorporation into the final document to maintain scholarly integrity of this research.

Digital Accessibility Disclosure Statement

In the preparation of this thesis, the following digital accessibility tools were used to ensure this document complies with federal requirements: Adobe Acrobat Pro Accessibility Checker. The author acknowledges full responsibility for the intellectual content of this work and has made a good faith effort to comply with digital accessibility requirements in publishing, wherein the nature of the content does not significantly change in order to do so. Furthermore, all content has been reviewed and revised to meet these requirements prior to final publication.

Acknowledgments

I would like to express my deepest appreciation to my advisor, Dr. Nek Sharan, for constant and invaluable guidance throughout my Masters study. Working with him has been a formative experience in learning how to ask good questions, pursue rigorous evidence, and develop a habit of critical thinking. I am also grateful to my committee members, Dr. Brian Thurow and Dr. Vrishank Rahgav, for their thoughtful feedback and encouragement, which strengthened this work at every stage.

I am indebted to colleagues Ganesh Dhungana, Minhazul Islam, Uday Shankar Howlader, and Sandip Adhikari in Computational Fluid Lab for their encouragement and feedback. Thanks are due to Postdoctoral Fellow Vikas Bhargav at Applied Fluids Research Group for the valuable discussion and feedback. I thank the members of the Combustion Physics Laboratory, the Applied Fluids Research Group, and the Advanced Flow Diagnostics Laboratory for many helpful discussions and practical assistance.

This research was supported by an Early Stage Innovations (ESI) grant from NASA's Space Technology Research Grants Program (Grant No. 80NSSC24K0278). I also acknowledge our technical Point of Contact, Dr. Wesley Chambers (NASA Marshall Space Flight Center), for his constructive guidance, and thank Dr. Ashley Korzun (NASA Langley Research Center) and Dr. Gregory Shallcross (NASA Jet Propulsion Laboratory) for their valuable insights throughout the project. The computational aspects of this work benefited from the Advanced Cyberinfrastructure Coordination Ecosystem: Services & Support (ACCESS) resources under grants PHY210037 and PHY240185 in support of the NASA-80NSSC22M0050 award, as well as the Auburn University Easley Cluster. Their assistance and resources were crucial for training and testing the neural-network models used herein.

Finally, With profound respect and gratitude, I thank my father Rajan Prasad Satyal and my mother Rama Satyal for their sacrifices and unwavering belief in me and my wife, Sajina

Bhattarai, for her love, patience, and steady encouragement, and my friends for their companionship and support. Whatever merits this thesis has are due in large part to them; any remaining shortcomings are mine alone.

Table of Contents

List of Tables

List of Figures

Chapter 1

Introduction

In recent times, substantial efforts have been directed at human expeditions to the Moon, Mars, and further. Missions aimed at planetary exploration, such as NASA's Artemis mission and SpaceX's Mars mission, represent a few examples of these endeavors. The primary aim of these missions is to expand human presence on other celestial bodies. Currently, the sole mode of transportation to these planets involves rocket engines that expel hot exhaust plumes to produce the thrust necessary for various mission tasks. Nevertheless, this transportation method has significant drawbacks due to the interaction between the exhaust plume from the rocket nozzle and the surfaces of extraterrestrial terrains, a phenomenon known as plume surface interaction.

In extra-planetary missions, the interaction between a lander's exhaust plume and the surface, known as plume-surface interaction (PSI), is a complex multi-physics issue involving the dynamics of the plume, the formation of craters in the regolith, and the flow of ejected material. As a lander descends or ascends, the exhaust plume can liberate rocks, gravel, soil, and dust, collectively referred to as ejecta, from the ground which then form craters beneath the lander. This ejecta poses a threat by potentially damaging the lander or nearby equipment. An occurrence of this was noted with Surveyor III, where small pits caused by granular ejecta were observed after the Apollo 12 landing [4]. During the Apollo 15 descent, the plume-surface interaction generated a cloud of ejecta that reduced visibility, leading to a landing on the edge of a shallow lunar crater with an 11-degree tilt. Had the tilt increased by 4 degrees, the lander wouldn't have been able to return to space[5]. Craters formed during this plume-regolith interaction can also destabilize rockets. These incidents highlight the challenges and concerns associated with landing large rockets on lunar and Martian surfaces.

A fundamental understanding of PSI is crucial to mitigating the issues mentioned above. Generally, it is unclear which underlying interaction mechanisms (erosion mechanisms) affect the PSI across different nozzle flow and ambient conditions. Plume dynamics, cratering, and ejecta flow are fundamentally coupled [3], as each process impacts the others. For instance, the crater formed by the plume determines the ejecta flow, which subsequently mixes with the plume and affects the cratering process. Analyzing how the crater profile evolves under varying nozzle flow and ambient conditions can offer insights into the underlying interaction mechanisms. This thesis seeks to explore the cratering process with the ultimate aim of developing a model capable of predicting this process. A detailed review of the literature highlights various erosion mechanisms, approaches to cratering modeling, and previous research efforts to comprehend them. Subsequently, the thesis outlines its specific objectives and motivations.

1.1 Literature review

1.1.1 Erosion mechanism

During impingement of the plume on the granular surface, some of the flow may either turn parallel to the surface, cause downward movement of the soil in bulk, or penetrate through the surface. In the first case, when the impinging flow cannot penetrate the surface and the stagnation pressure is less than the bearing capacity of the soil, the flow direction turns parallel to the surface. When the flow moves parallel to the surface, it exerts aerodynamic forces on the granular materials/particles on the surface. These aerodynamic forces are the lift and drag forces on the particles. The aerodynamic drag force, when it exceeds the interparticle forces of the materials holding it on the surface, causes the materials to be carried away by the flow, causing the surface to erode[6][7]. This type of erosion is called viscous erosion and occurs at the top layers of the surface, creating a parabolic or series of parabolic-type crater profiles. Viscous erosion is the dominant mechanism on the moon, due to the moon's low ambient pressure that causes the plume to get highly expanded, distributing the force over a large surface, resulting in mild impingement pressure [8].

Similarly, when the stagnation pressure of the impinging gas plume exceeds the bearing capacity of the granular bed, it results in mechanical loading that shears the surface and pushes it downward, perpendicular to the soil surface[9]. This downward movement of soil in bulk causes the formation of a narrow, cylindrical-type crater, which continues to grow until the plume flow weakens such that the stagnation pressure of the plume becomes less than the bearing capacity of the soil[8]. This type of cratering mechanism is called bearing capacity failure[10].

However, when the soil is highly permeable, it causes a different cratering mechanism called Diffusion Driven Flow (DDF). In DDF, the impinging plume penetrates the soil surface, imparts drag forces on the particles below the surface, and moves soil grains through the subsurface[9].

The next mechanism, known as Diffused Gas Eruption (DGE), occurs when the impinging plume increases the sub-surface pressure. While the plume is active, this pressure is contained beneath the surface. Once the plume stops, the sub-surface pressure exceeds both the ambient pressure above the surface and the weight of the soil, causing the permeated soil to flow back toward the surface and erupt outward[11]. All erosion mechanisms, except viscous erosion, such as bearing capacity failure, diffusion-driven flow, and diffused gas eruption, are fast cratering mechanisms. Broadly, it is unclear which mechanisms dominate under different flow and soil conditions.

Various crater geometries and their transitions can be associated with different erosion mechanisms. Small-scale experiments (e.g., [12] [13] [14]) have reported that prolonged subsonic jet impingement forms a composite crater (an outer conical and an inner parabolic) in which depth grows logarithmically in time. Metzger *et al.* [15][12] mention that such crater growth is driven by viscous erosion, the primary mechanism in lunar landings. Metzger *et al.* [13] identified two different mechanisms, which are bearing capacity failure and diffused driven flow, for high-velocity jets causing deep cratering.

Identifying crater geometry and the underlying mechanisms is important for developing predictive models and scaling laws for PSI at reduced pressures. Therefore, my thesis develops the methodology to extract and identify different crater geometry with the ultimate goal of identifying the physical mechanism driving the erosion.

1.1.2 Crater modeling

Several studies have proposed semi-empirical relationships and scaling laws to model crater evolution. Either crater depth (D), width (W), volume (V), or all are modeled with time when describing crater evolution. Donahue et al. [16] and Metzger et al. [13] employed a logarithmic fit given by $D(t) = a\log(bt + 1)$ to model crater depth evolution over time. In the expression, D is the depth, t is the time, and a and b are fitting parameters that are linearly dependent on the nozzle height (h) and $\rho_g v^2 d_e/h^\alpha$ respectively, where ρ_g is the density of gas, v is the velocity of the jet, d_e is the jet exit plane diameter, and α denotes the value estimated from the data. However, these functional forms primarily describe parabolic-type craters (parabolic and conical–parabolic.) observed in specific experimental conditions. For example, Metzger et al. [12] and Stubbs et al. [17] mainly discuss the depth and volume evolution of parabolic-type profiles.

LaMarche and Curtis [6] argued that an arctangent equation, given by $D(t) = a_1 \tan^{-1}(b_1 t^{c_1})$ (a_1, b_1, and c_1 are fitting parameters), could be fitted to initial crater depth growth in the experimental data and extrapolated to estimate the asymptotic or steady-state crater depth for various particle properties (size, density, and shapes). Stubbs et al. [17] compared both logarithmic and arctangent models to describe the evolution of crater width and depth across varying nozzle heights and found that the arctangent fit performs better for lower nozzle heights due to rapid depth growth. They also used a power-law model, given by $V(t) = \beta t^\gamma$ (β and γ are fitting parameters obtained from experimental data), to represent crater volume evolution.

Gorman et al. [18] developed a power-balance model, inspired by an energy-based impact cratering model, that relates crater depth to the kinetic energy of the impinging jet. They proposed the following expression for modeling crater depth evolution:

$$D(t) = f^{1/3}(\xi,\eta)t^{1/3}\left[\frac{f(\xi,\eta)t}{(C_0^{-6/\zeta} f^{\zeta}(\xi,\eta)t^{\zeta} + D_0^{\zeta} C_0^{-6/\zeta})^{1/\zeta}}\right]^{2/3}. \tag{1.1}$$

Here, $f(\xi, \eta)$ and $g(\xi, \eta)$ measure the erosion rates, where ξ represents granular properties (e.g., particle size and density, interparticle cohesion, and soil compaction), and η includes gas-phase properties (e.g., mach number, flow rate, gas density, nozzle height, nozzle width, ambient pressure, and jet pressure). Similarly, $C_0 = g(\xi, \eta)/f^{1/3}(\xi, \eta)$ is the erosion rate ratio. Their model fits early-stage crater depth evolution as a linear relationship with time $(D(t) = f(\xi, \eta)t)$ and the late-stage crater depth as a $1/3$ power law $(D(t) = C_0 f^{1/3}(\xi, \eta)t^{1/3})$ across a wide range of granular compositions, mass flow rates, and nozzle heights. The critical depth (D_0) and C_0 were obtained from each dataset. However, the model does not address the terminal asymptotic crater depth growth and diverse crater shapes (*e.g.* annular, conical annular profile etc.).

More recently, Bruni et al. [19] applied the symbolic regression framework PySINDy to extract a set of ordinary differential equations from experimental cratering data for identifying crater depth and width evolution rates with simple analytical forms:

$$\frac{dD}{dt} \approx \sum_{i=1}^{2} (\Phi_{i,D} D^{i-1}) \tag{1.2}$$

$$\frac{dW}{dt} \approx \sum_{i=1}^{2} (\Phi_{i,W} W^{i-1}) \tag{1.3}$$

Here, D and W are the crater depth and width, and $\Phi_{i,D}$ and $\Phi_{i,W}$ are the coefficients obtained from the SINDy approach. These time derivatives were integrated to determine the evolution of crater depth and width with time. However, this data-driven model considers only five experimental cases with parabolic crater profiles, ignoring crater evolution across different shapes and operating conditions.

Metzger [15] and Dotson et al. [20] proposed a volumetric erosion rate model for viscous erosion as

$$\frac{dV}{dt} = 2\pi \frac{\rho_e U_e^2 A_e}{\rho_p g d_p + f(C)} \tag{1.4}$$

where the erosion rate represents the ratio of the total kinetic energy of the gas to the combined potential and cohesion energy of the surface. The proposed rate is valid for steady-state conditions, under which the crater volume evolves linearly with time, and the crater volume can be obtained by integrating the equation. However, Gorman et al. [18] observed that crater diameter evolution increases linearly during the early stage and transitions to sub-linear growth at later times, indicating the need to incorporate non-linear temporal effects in modeling crater evolution.

Across the above-mentioned studies, the evolution of crater geometry is typically represented by prescribing a specific functional form for the temporal dynamics, such as logarithmic, arctangent, or power-law relationships. In these formulations, the fitting parameters implicitly depend on the operating conditions governing the plume–surface interaction, including nozzle height, jet momentum, ambient pressure, and soil properties. Furthermore, the linear and sub-linear growth behaviors represented in these models describe only specific growth regimes and do not fully capture the broader range of crater evolution observed in experiments. Although these models capture certain regimes of crater growth, the assumed functional forms restrict their applicability across different crater morphologies (e.g., annular, parabolic, conical–parabolic, conical deep, conical–annular, etc.) and operating conditions.

The structure of the above models suggests an implicit separation between the temporal dynamics of crater growth and the dependence of the model parameters on the operating conditions. In each case, a specific temporal functional form (e.g., logarithmic, arctangent, or power-law) is prescribed, while the fitting parameters implicitly describe the influence of nozzle height, jet momentum, ambient pressure, and granular properties. Building on this idea, a more general modeling framework can be obtained by explicitly separating the temporal evolution from its parametric dependence. Such a decomposition between temporal dynamics and parametric dependence is commonly used in reduced-order modeling and surrogate modeling of dynamical systems. In these approaches, the system response is expressed as a combination of temporal basis functions whose coefficients depend on the system's operating parameters [21]. Owing to the current literature on crater modeling, Crater evolution can also be interpreted in terms of the volume erosion rate as,

$$\frac{dV}{dt} = F(t, \beta), \tag{1.5}$$

where $V(t)$ denotes crater volume, t is time, and β represents the operating parameters governing the plume–surface interaction. Integrating this relationship indicates that crater evolution depends on both the temporal dynamics of erosion and the governing operating conditions. Upholding the idea of the separation of temporal dynamics and parametric dependence, the crater volume (V) based on erosion rate dynamics can be written as

$$V(t, \beta) = \sum_{k=1}^{K} c_k(\beta)\, \phi_k(t), \tag{1.6}$$

where $\phi_k(t)$ are basis functions describing the temporal dynamics and $c_k(\beta)$ are coefficients that depend on the operating parameters β governing the system behavior. This formulation separates the temporal evolution from the parametric variability of the system while retaining the ability to capture nonlinear responses.

Polynomial representations have been widely used to model nonlinear dynamical systems and parametric dependencies. In reduced-order modeling, system dynamics are often represented as combinations of temporal or spatial basis functions, with coefficients that depend on operating parameters [21]. Sparse identification of nonlinear dynamics (SINDy) similarly represents system evolution using a polynomial basis to model nonlinear behavior directly from data [22]. Response-surface methodologies provide a way to approximate system responses using polynomial functions of the parameters [23]. These approaches demonstrate the effectiveness of polynomial bases in representing nonlinear relationships between system dynamics and operating parameters.

Motivated by this general modeling framework, the present work represents crater evolution using a polynomial basis in time. In this formulation, the crater geometry (i.e. volume) is expressed as

$$V(t, \beta) = \sum_{k=0}^{K} c_k(\beta)\, t^k, \tag{1.7}$$

where t denotes time and $c_k(\beta)$ are polynomial coefficients that depend on the operating parameters (β) governing the plume–surface interaction. The coefficients $c_k(\beta)$ are further modeled as polynomial functions of β, consistent with response-surface and polynomial-surrogate practices. By representing temporal evolution using a polynomial basis and modeling the coefficients as functions of the operating parameters, this formulation provides a flexible framework for modeling different crater growth regimes. Consequently, the proposed representation extends existing semi-empirical crater evolution models by allowing the temporal behavior to adapt systematically to varying operating conditions.

1.2 Motivation and objectives

To improve understanding of Plume Surface Interaction (PSI) and predictive capabilities, the NASA Game Changing Program's PSI project conducted PFGT experiments. The PFGT campaign has two objectives: (i) PFGT1–aimed at studying the supersonic cratering and ejecta dynamics by evaluating the crater geometry and ejecta velocities under ambient pressures ranging from lunar to martian, and (ii) PFGT2–aimed at visualizing the supersonic impinging plume and measuring the surface pressures in reduced atmospheric conditions.[3]. The objectives of this thesis are centered around data obtained from NASA's PFGT1 PSI experiment.

To understand the underlying mechanism of erosion, this work develops a methodology to extract crater geometry from a cratering experiment and classify craters based on their shapes. In addition, to address the limitations of generalized model, this work explores the use of polynomial reduced order model, that model the crater evolution as $V(t) = \int F(t, \beta) dt$, where V is the crater volume, β is the operating conditions such as nozzle height (h/d_{e}), ambient pressure (p_{amb}), mass flow rate ($\dot{m}$), etc, and time (t). The primary objective of the thesis is to develop a model to predict cratering dynamics under various operating conditions (mass flow rate, ambient pressure, and nozzle height), while the secondary objective is to develop tools to extract and classify crater geometry from plume-surface interaction experimental videos. The motivation driving these research goals is outlined as follows:

1. Developing a machine learning–based image-extraction method to obtain crater geometry from plume–surface interaction experiments offers a flexible and experiment-agnostic approach, allowing straightforward adaptation to new setups.

2. Automating crater-shape classification will enable rapid, consistent labeling of crater shapes, ultimately supporting the identification of underlying erosion mechanisms.

3. Investigating data-driven machine learning model as predictive models for cratering dynamics under various operating conditions will assist in developing a reduced-order model. This model can forecast crater behavior across diverse scenarios and helps in sensitivity analysis allowing to investigate impact of different operating parameter on cratering dynamics.

1.3 Accomplishments

The following accomplishments were achieved for the first time using data from NASA's PSI experiments.

1. Introduced an innovative deep neural network framework to automatically extract crater boundaries and outline profiles from high-speed PFGT1 cratering videos for the first time.

2. Designed a convolutional neural network (CNN) to automatically categorize crater geometries into specific shapes: parabolic, annular, conical-parabolic, conical-annular, and conical-deep.

3. A data-driven, temporally and parametrically separable framework for modeling crater geometry as it evolves over time and across different operating conditions. This polynomial model is trained on PSI experimental data to forecast the temporal progression of crater growth.

1.4 Framework

The objectives of this thesis are pursued using cratering datasets from the Plume-Surface Interaction (PSI) experiments conducted in the 15-foot vacuum chamber at NASA's Marshall Space Flight Center. An overview of the experimental campaign is presented in Chapter 2. Chapter 3 details the neural-network methods for crater-geometry extraction, crater-shape classification, and modeling crater evolution. Chapters 4 and 5 report the evaluation results of the machine-learning models for crater geometry extraction and shape classification, and crater modeling, respectively. Finally, Chapter 6 concludes with a summary of key findings and outlines directions for future research.

Chapter 2

Physics Focused Ground Test's (PFGT) experiment overview

2.1 Experimental setup

The PFGT campaign experiment was carried out at NASA Marshall's 15' vacuum chamber to achieve lunar/martian ambient environment [3]. The basic configuration of the experimental setup consists of a regolith simulant container, support structure, nozzle (diameter ($\bar{d}_{\mathrm{e}} = 1.38$ cm), and diagnostics system. The regolith simulant container has a splitter plate and a transparent acrylic viewing pane, as shown in Figure 2.1, allowing for the 2-D visualization of crater formation and ejecta flow [1]. A supersonic Nitrogen gas simulant was bisected by a splitter plate to impinge on the regolith bed. The resulting cratering and ejecta dynamics were captured by crater and ejecta cameras, respectively. The diagnostic system is depicted in figure 2.1. The data investigated in this thesis were obtained by the crater camera.

Table 2.1: Operating parameter ranges.[1, 2]

Parameter	**Range**
$\bar{h}/\bar{d}_{\mathrm{e}}$	3.0 to 13.0
$\bar{p}_{\mathrm{amb}}$	2.67 Pa to 600 Pa (0.02 torr to 4.5 torr)
$\bar{\dot{m}}$	0.32 g/s to 8.6 g/s

The parameter space in the PFGT experiments spans various mass flow rates ($\bar{\dot{m}}$), nozzle height to diameter ratios ($\bar{h}/\bar{d}_{\mathrm{e}}$), initial ambient pressures ($\bar{p}_{\mathrm{amb}}$) and regolith types. Six different regolith simulants were used to model the lunar and martian surfaces, namely Mono-Disperse Sand (MDS), Lunar Simulant (BP-1), Irregular Mixture (IRR), Bi-Disperse Sand (BDS), Tri-Disperse Sand (TRI), and Mono-disperse Glass Beads (MGB). The range of parameters in the experiments is given in Table 2.1. In addition, the composition of different

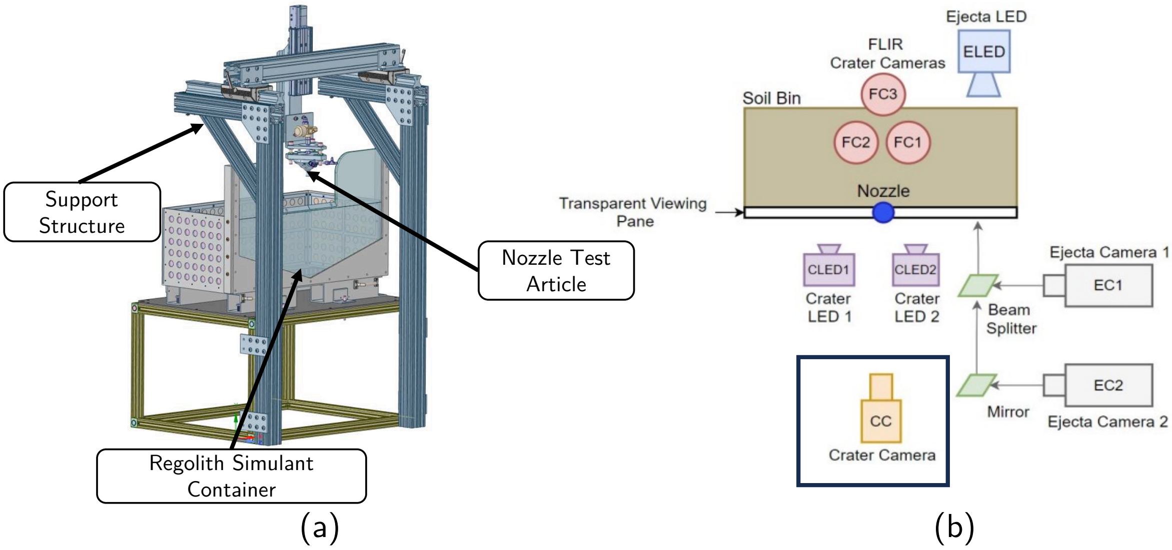

Figure 2.1: Experimental setup showing (a) regolith simulant container with splitter plate [2] (b) low to ultra high-speed diagnostic system with crater and ejecta cameras [3].

regolith simulants is tabulated in Table 2.2. The plume consists of heated N_2 gas at a total temperature of 500 K and a nozzle exit Mach number of 5.3 [2].

Table 2.2: Regolith simulant types for PFGT1.[1, 2]

Type	Material	Specifications
Mono-disperse Sand	Silica Sand Grains	sieved to $\bar{d}_{\rm p} \approx 150\ \mu$m nom
Lunar Simulant	Black Point-1	full range mfg. spec
Irregular Mixture	Black Point-1	sieved to $\bar{d}_{\rm p} \approx 350\ \mu$m nom
Bi-disperse Sand	Silica Sand	$\bar{d}_{\rm p} \approx 50\ \mu$m nom + MDS, 50/50% by vol.
Tri-disperse Sand	Silica Sand, BP-1	BDS + IRR, 33/33/33% by vol.
Mono-disperse Glass Beads	Soda Lime Glass Beads	$\bar{d}_{\rm p} \approx 150\ \mu$m nom

2.2 Non-dimensionalization

Variables and operating parameters are non-dimensionalized by nozzle diameter ($\bar{d}_{\rm e}$) as the reference length scale and jet-exit velocity ($\bar{U}_{\rm e}$) as the velocity scale for modeling crater evolution. The non-dimensional variables are listed below.

$$
\begin{aligned}
V &= \frac{\bar{V}}{\bar{d}_{\rm e}^3} \qquad & t &= \frac{\bar{t}}{\bar{d}_{\rm e}/\bar{U}_{\rm e}} \qquad & h/d_{\rm e} &= \frac{\bar{h}}{\bar{d}_{\rm e}} \\
p_{\rm amb} &= \frac{\bar{p}_{\rm amb}}{\bar{p}_{\rm e}} \qquad & \dot{m} &= \frac{\bar{\dot{m}}}{\bar{p}_{\rm amb}\bar{d}_{\rm e}^2/\bar{U}_{\rm e}} & &
\end{aligned}
\tag{2.1}
$$

The dimensional variables are denoted with an overbar. From the experiments, $\bar{d}_e = 1.38\times10^{-2}$ m, $\bar{U}_e = 939.7$ m/s, $\bar{p}_e = 49.7$ Pa at $\bar{\dot{m}} = 0.32$ g/s, and $\bar{p}_e = 1336$ Pa at $\bar{\dot{m}} = 8.6$ g/s.

2.3 Experimental Data summary

2.3.1 Cratering image

The crater camera from the PFGT campaign (NASA Marshall 15' vacuum chamber) yields high frame rate recordings of 2-D cross-sections of the crater through an acrylic window. It captures the crater evolution over a test time of 10 seconds at roughly 5000 frames per second [3]. A total of 83 experimental runs were performed, including repeated runs at some parameter spaces (dataset obtained from the NASA TechPort portal [24]). Each experimental video consists of a greyscale image of a crater.

As discussed in the literature section, the crater geometry, characterized by its shape, height, and diameter, is associated with the underlying erosion mechanism, e.g., viscous erosion, bearing capacity failure, etc. [12]. Figure 2.2 shows the various crater shapes (namely, parabolic, annular, conical-parabolic, conical-annular, and conical-deep) observed in the experiments.

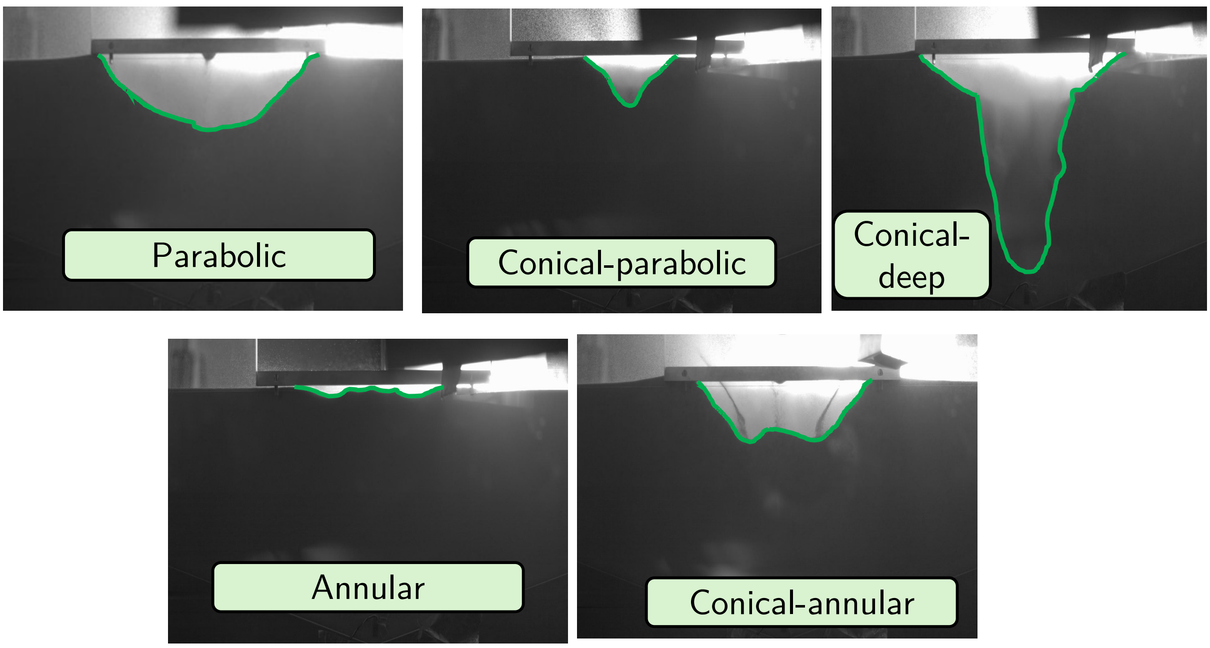

Figure 2.2: Different crater shapes observed in the experiments.

Visual appearance varies across runs due to illumination and optics (occasional glare), and regolith reflectivity and grain shape (bright MDS/MGB vs. darker BP-1/IRR). Typical artifacts include contrast fluctuations, ejecta haze, and transient window fouling as shown in the Figure 2.3. These artifacts make the extraction of crater geometry from the frame images of the cratering videos challenging. Of the 83 runs, only 55 have some crater visibility (the strong ejecta completely obscures the view of the crater in the remaining cases); therefore, the crater grometry extraction in this thesis is restricted to those 55 cases. The parameter values for those cases are provided in the Appendix A. The images are subsampled at 25 frames per second for faster work iteration (crater extraction and modeling) and have resolutions of 1280×800, 1088×752, or 1088×650.

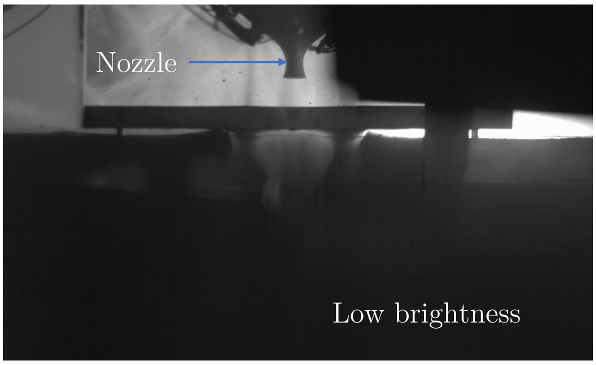

(a)

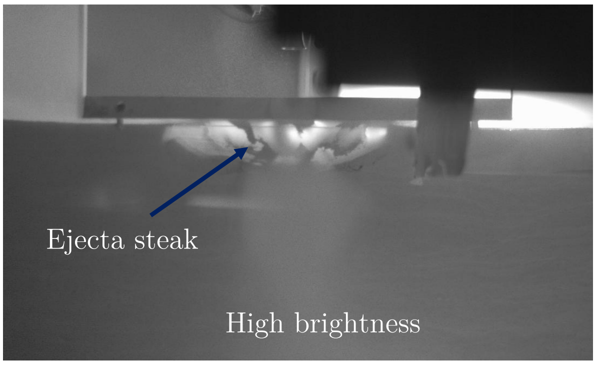

(b)

Figure 2.3: Frames from PFGT videos showing differences in image contrast and details.

2.3.2 Temporal evolution of crater geometry

Across the experimental ranges of $\bar{h}/\bar{d}_\mathrm{e}$, $\bar{p}_\mathrm{amb}$, $\bar{\dot{m}}$, and regolith type, evolution follows a common sequence: (i) onset of cratering; (ii) transient cratering with shape transitions ; (iii) steady crater growth or crater collapse. With time, the maximum depth, maximum width (near the surface), volume, etc., of the crater change, and this cratering phenomenon is unique to a given set of operating conditions. An example of the crater volume evolution across different parameter space is shown in the Figure 2.4. It can be observed that the early time volume growth is similar across runs, followed by divergence driven primarily by ambient pressure and nozzle height (mass flow rate remains the same). The higher $\bar{p}_\mathrm{amb}$ and smaller $\bar{h}/\bar{d}_\mathrm{e}$ in Run 13 strengthen plume regolith interaction, resulting in the largest volume, whereas the larger $\bar{h}/\bar{d}_\mathrm{e}$ in Run 21 weakens impingement and produces the smallest growth. The late time concavity of the volume evolution indicates a reduced growth rate as the crater enlarges, suggesting that the crater formation gradually approaches a quasi-steady regime. As we account more operating parameter into account, it will be more difficult to establish the relationship of the crater evolution. Therefore, a reduced order model infered by cratering dynamics is required to model the relationship of evolution dynamics across varying parameter space.

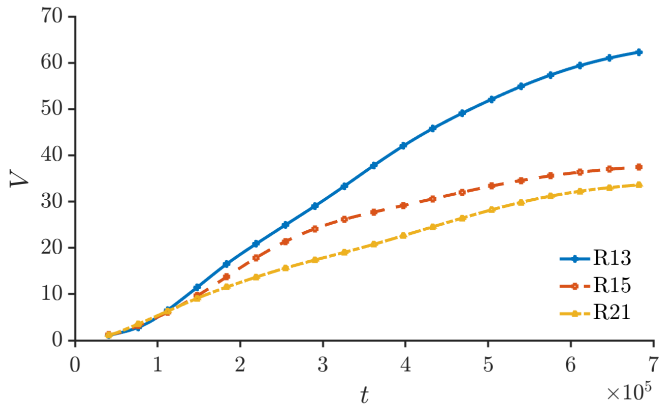

Run	$\bar{p}_\mathrm{amb}$ (torr)	$\bar{h}/\bar{d}_\mathrm{e}$	$\bar{\dot{m}}$ (g/s)
R13	4.5	10	0.32
R15	2.003	10	0.32
R21	2.003	13	0.32

Figure 2.4: Non-dimensionalized crater volume evolution (left) and corresponding run parameters (right).

Several distinct modes of temporal evolution were observed in the experimental videos, depending on the mass flow rate, ambient pressure, and nozzle height for the MDS soil types. Specifically, we noted changes in the time history of crater development and shifts in the overall evolution pattern under different operating conditions. These transition regions exhibit sharper temporal changes and increased sensitivity to operating parameters, and they are therefore expected to be the most difficult regimes for modeling with sparse operating-parameter sampling. To demonstrate this, we have discussed the transitions identified when varying a single parameter while keeping the others fixed.

Fixed mass flow rate and nozzle height

Figure 2.5(a-c) depicts the transitions observed at different ambient pressures for a fixed mass flow rate of 0.32 g/s and a nozzle height of 10. At an ambient pressure of 0.02 torr, the crater profile evolves with annular geometry. For ambient pressures of 2 and 4.5 torr, the crater shape

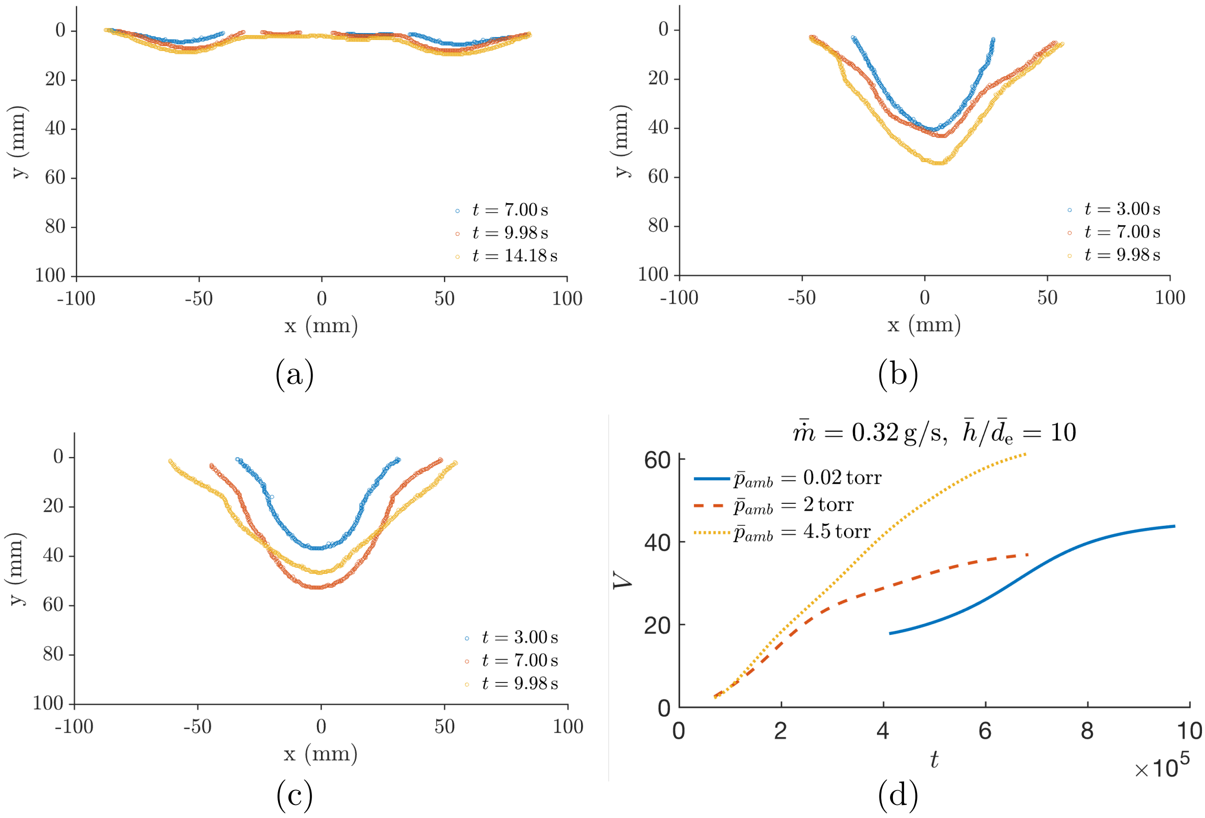

Figure 2.5: Crater shape transitions for fixed $\bar{m} = 0.32$ g/s, $\bar{h}/\bar{d}_\mathrm{e} = 10$, (a) $\bar{p}_\mathrm{amb} = 0.02\,\mathrm{torr}$ (b) $\bar{p}_\mathrm{amb} = 2\,\mathrm{torr}$ and (c) $\bar{p}_\mathrm{amb} = 4.5\,\mathrm{torr}$ (d) Temporal evolution of crater volume at different ambient pressure.

evolves from parabolic to conical parabolic. Figure 2.5(d) presents the temporal evolution of the volume for these transitions. As the ambient pressure rises, the volume–time curves scale up. Furthermore, the conical parabolic profile approaches its asymptotic volume more quickly at lower ambient pressures than at higher ambient pressures.

Fixed mass flow rate and ambient pressure

Figure 2.6(a-e) shows the sequence of transitions observed at different nozzle heights for a constant mass flow rate of 0.32 g/s and an ambient pressure of 0.02 torr. At nozzle heights of 5 and 6, the crater profile changes from an annular shape to a parabolic one. For nozzle heights of 8, 10 and 13, the crater shape evolves into annular shape. In summary, with increasing nozzle height, the crater shape progresses from annular to parabolic, then to annular profile. This sequence of shape changes is reflected in the evolution of crater volume shown in Fig. 2.6(f).

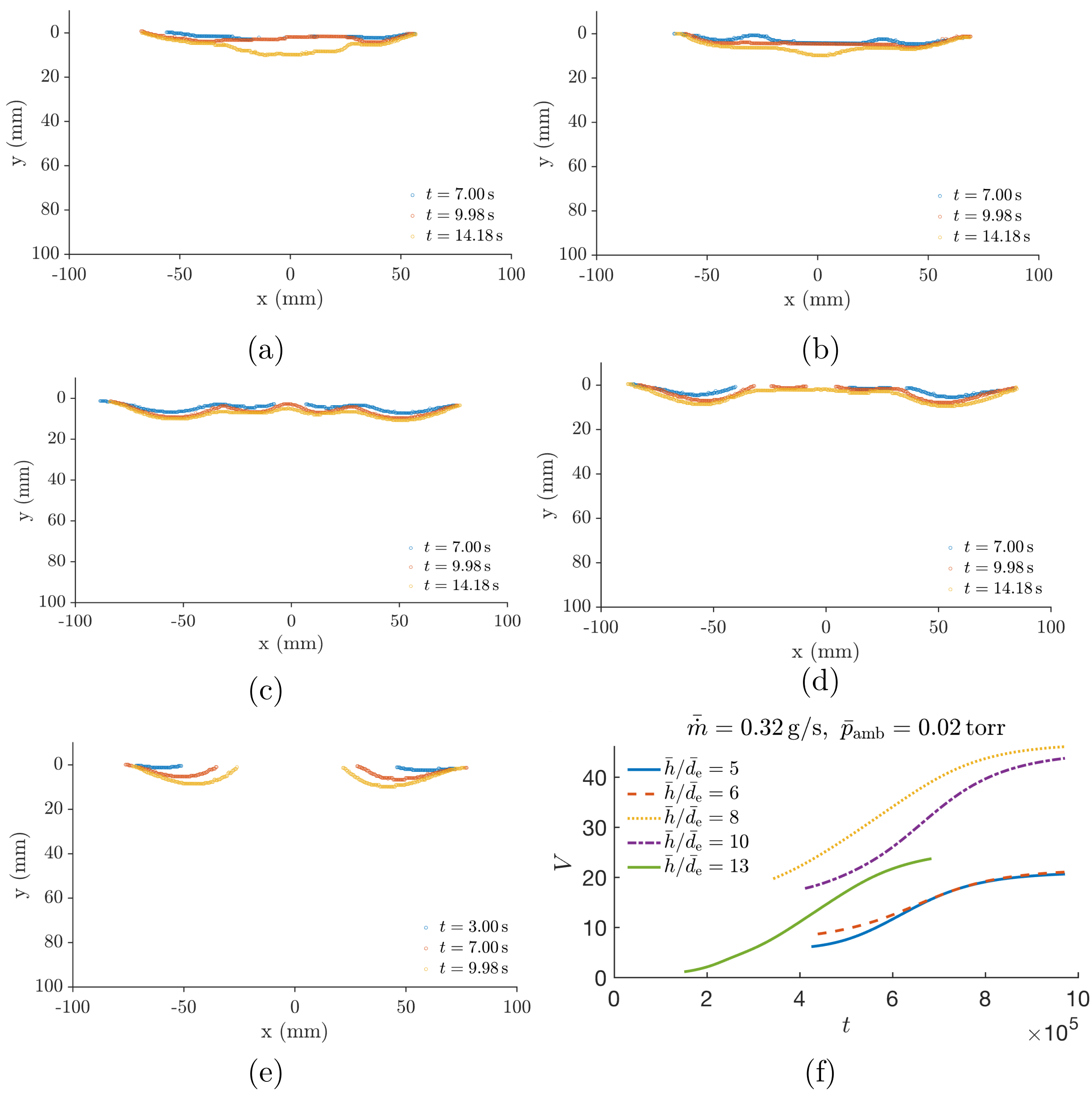

Figure 2.6: Crater shape transitions for fixed $\bar{\dot{m}} = 0.32$ g/s, $\bar{p}_{\mathrm{amb}} = 0.02\,\mathrm{torr}$, (a) $\bar{h}/\bar{d}_{\mathrm{e}} = 5$ (b) $\bar{h}/\bar{d}_{\mathrm{e}} = 6$ (c) $\bar{h}/\bar{d}_{\mathrm{e}} = 8$ (d) $\bar{h}/\bar{d}_{\mathrm{e}} = 10$ and (e) $\bar{h}/\bar{d}_{\mathrm{e}} = 13$ (f) Temporal evolution of crater volume at different heights.

In this evolution plot, the crater volume initially grows with nozzle height up to $h/d_e = 8$, beyond which the curves shift to lower values as the height increases further. This change in the volume trend is likely linked to the corresponding transitions in crater shape with nozzle height.

Fixed ambient pressure and nozzle height

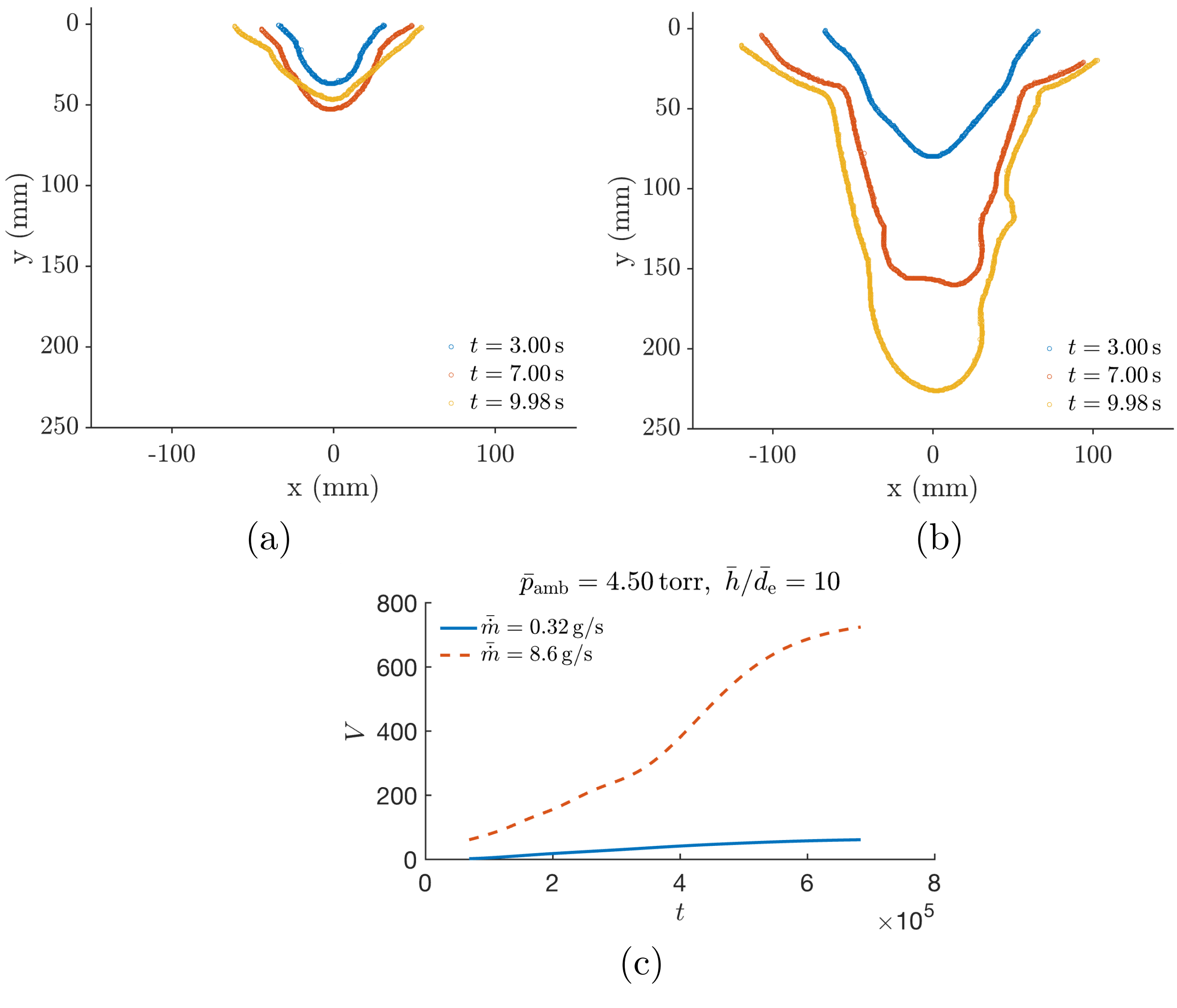

Figure 2.7: Crater shape transitions for fixed $\bar{p}_{\mathrm{amb}} = 4.5\,\mathrm{torr}$, $\bar{h}/\bar{d}_{\mathrm{e}} = 10$, (a) $\bar{\dot{m}} = 0.32$ g/s and (b) $\bar{\dot{m}} = 8.6$ g/s (c) Temporal evolution of crater volume at different mass flow rate.

Figure 2.7(a-b) presents the transitions observed at different mass flow rates for an ambient pressure of 4.5 Torr and a nozzle height of 10. At a mass flow rate of 0.32 g/s, a transition from a parabolic to a conical parabolic profile is observed. In contrast, at a mass flow rate of 8.6

g/s, the profile changes from parabolic to conical deep. The corresponding evolution of the volume during these transitions is depicted in Figure 2.7(c). It appears that the volume scaling shifts in proportion to the mass flow rate. However, this proportionality cannot be conclusively confirmed due to the limited number of available mass flow rate data points.

Chapter 3

Methodology

Conventional edge detection approaches, such as the Canny algorithm, can be used to extract crater edges from cratering images. However, it fails to provide accurate edges for images shown in figure 2.3 because of ejecta streak and brightness differences in the images, and may detect additional edges (noises), as shown in figure 3.1. Therefore, edge detection methods tailored to specific configurations are desired, as existing approaches are ineffective across diverse scenarios.

With the development of machine learning and artificial intelligence, new edge detection algorithms are being developed in the field of digital image processing. A machine learning algorithm can be supervised, where the models are trained on labeled data sets, or unsupervised, where the model detects edges without any labeled data sets [25]. In this thesis, I focus on

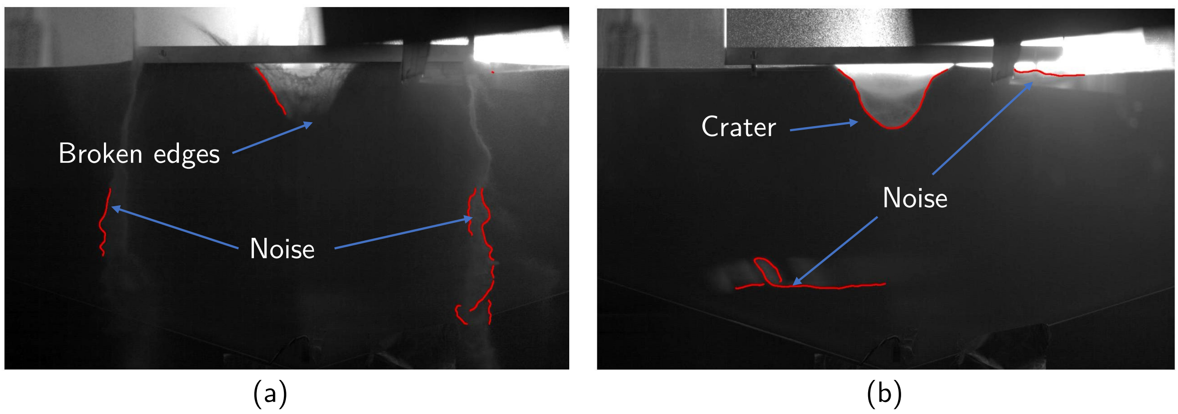

Figure 3.1: Issues with the Canny edge detection – broken edges and noise.

training and developing a supervised machine learning method for edge-based crater identification that uses the edges identified from the Canny algorithm and Segment Anything Model 2 (SAM2)-generated masks [26] as ground truths for training and performance evaluation.

3.1 Convolutional Neural Network (CNN) for crater geometry extraction

Convolutional Neural Network (CNN) is a deep learning architecture inspired by the biological processes in an animal's visual cortex [27]. The major components of CNN are convolution, pooling, and activation layers. Each convolution layer consists of a convolution kernel of size $m \times m$ (typically $m = 1$, $m = 3$, or 5), which performs a convolution operation on an image to extract features or patterns such as edges, textures, etc., and provides feature maps as output. The input images are represented by a $C \times H \times W$ matrix containing pixel values $(0 - 255)$, where C represents the channel of input images, *e.g.*, $C = 3$ represents the Red-Green-Blue channel of the input image, H and W are height and width of the image, respectively. The convolution operation in a CNN layer can be expressed as

$$Op_{i,j}^{(k)} = \sum_{c=1}^{C} \sum_{u=0}^{m-1} \sum_{v=0}^{m-1} Wt_{c,u,v}^{(k)} \cdot Ip_{c,i+u,j+v} + b^{(k)}, \tag{3.1}$$

for $k = 1, 2, \ldots, K$ where

- $Ip \in \mathbb{R}^{C \times H \times W}$ is the input tensor (image or feature map) with C channels.
- $Wt^{(k)} \in \mathbb{R}^{C \times m \times m}$ is the convolution kernel for the k-th output feature map.
- $b^{(k)} \in \mathbb{R}$ is the bias for the k-th feature map.
- $Op^{(k)} \in \mathbb{R}^{H' \times W'}$ is the resulting output feature map after applying the k-th kernel.
- m is the kernel size (typically 1, 3, or 5).
- (i, j) indexes the spatial location in the output.
- K is the number of output feature maps (i.e., number of convolution filters).

In equation 3.1, Weights (Wt) and bias (b) are the learnable parameters that are optimized during the neural network training process. Next, the pooling layers reduce the dimensions of the input feature map (output of the convolution layer), which in turn decreases the size of the subsequent layers and, hence, the computational cost of training the network. It also helps reduce the problem of overfitting [28]. For a max pooling layer with a window size of $p \times p$, the operation is defined by

$$Of_{i,j}^{(k)} = \max_{\substack{0 \leq u < p \\ 0 \leq v < p}} Op_{s \cdot i+u,\, s \cdot j+v}^{(k)} \tag{3.2}$$

, where

- $Op^{(k)} \in \mathbb{R}^{H' \times W'}$ is the input feature map to the pooling layer for the k-th channel.
- $Of^{(k)} \in \mathbb{R}^{H'' \times W''}$ is the output pooled feature map.
- p is the pooling window size (e.g., 2×2).
- s is the stride of the pooling operation.
- (i, j) denotes the spatial location in the pooled output.
- $k \in \{1, 2, \ldots, K\}$ denotes the feature map index.

The input layer is followed by a series of convolution and pooling layers. The choice of the number and combination of such layers depends on task complexity, dataset characteristics, and feature extraction requirements [28], thus considered as a hyperparameter. Various activation functions, such as ReLU, tanh, sigmoid, etc., introduce nonlinearity in the CNN and help capture the nonlinear relationships in the feature maps [27]. Generally, in classification tasks, ReLU is used as the activation function in the inner layers after the pooling operation, and sigmoid in the output layer. Given an input feature map $Of^{(k)}$, the activation function $f(\cdot)$ is applied element-wise to produce the activated feature map $A^{(k)}$:

$$A_{i,j}^{(k)} = f(Z_{i,j}^{(k)}) \tag{3.3}$$

Common activation functions used in CNNs include (i) Rectified Linear Unit (ReLU), given by $f(x) = \max(0, x)$, (ii) Sigmoid given by $f(x) = 1/(1 + e^{-x})$, etc., where x is the input to the activation funct.ion

3.1.1 Labeled data generation for CNN-based crater geometry extraction

Labeled data generation using the Canny algorithm

The PFGT videos provide crater's evolution for various parameter values (or operating conditionAutomatedated classification of the crater shae.g.mple, parabolic, annular, deep cretc.) from the videos will help simplify the analysis of the highly parametric PFGT dat,aenabling the identificationtify modeling ofodel the erosion regime and mechanisms. Before the classification, however, the crater shape (defined by the spatial coordinates lining the crater boundary, as shown in figure 3.1(b)) needs to be determined. The conventional edge detection methods, such as the Canny algorithm, can provide erroneous edges (noise), as depicted in figure 3.1. The extent of the noise varies from one frame to another, therefore, tuning the parameters in the Canny algorithm to accurately capture the crater edge across all frames of a PFGT video is infeasible. Hence, a novel approach (that exploits the roughly parabolic nature of the crater edge and the fact that the crater edge gradually changes from one frame to another) is developed to eliminate the noise, as discussed below, yielding a clean crater profile.

Incorporating the parabolic profile condition: The edge data obtained from the Canny algorithm consists of point clusters with the crater profile and noise. To eliminate the noise, first, the roughly parabolic nature of the crater profile is incorporated in the crater detection algorithm. It is accomplished by sorting the data points (with coordinates $\left(x_j^k, y_j^k\right)$, where $1 \leq k \leq M$ and $1 \leq j \leq N_k$ with M denoting the number of clusters and N_k the number of points in the k-th cluster) in each cluster by the y-coordinate and indexing them accordingly. The point with the minimum y-coordinate is then considered as the origin and all coordinates $\left(x_j^k, y_j^k\right)$ are transformed w.r.t. this origin to $\left(\hat{x}_j^k, \hat{y}_j^k\right)$, where $\hat{x}_j^k = x_j^k - x_{\text{min}}^k$ and $\hat{y}_j^k = y_j^k - y_{\text{min}}^k$, and $\left(x_{\text{min}}^k, y_{\text{min}}^k\right)$ denotes the point in the k-th cluster with the minimum y-coordinate. In this transformed coordinate system with the points sorted by the y-coordinate, the parabolic profile requires that the x-coordinate of the points change sign after every few points, *i.e.*, $\hat{x}_j^k \cdot \hat{x}_{j+1}^k < 0$ after every few points, as shown in figure 3.2(c). Adding this condition, in conjunction with the time series condition (discussed next), helped identify the crater points and eliminate the noise.

Incorporating the time series character of the video frames: The PFGT videos provide the time evolution of crater geometry. The high frame rate ensures that the change in crater profile is small from one frame to another. Generally, the crater width changes more gradually than the depth. Hence, the extent of the crater edge in one frame acts as a reference to isolate the crater profile from noise in the next frame. To incorporate this time series character, the quantity

$$\mathcal{M} = \left|x_{\text{max}}^{n+1} - x_{\text{max}}^{n}\right| + \left|x_{\text{min}}^{n+1} - x_{\text{min}}^{n}\right| + \left|y_{\text{max}}^{n+1} - y_{\text{max}}^{n}\right| + \left|y_{\text{min}}^{n+1} - y_{\text{min}}^{n}\right| \tag{3.4}$$

where n is the frame number, is evaluated for each cluster in a frame. The cluster with the minimum $\mathcal{M}$ is, typically, the crater edge.

The overall algorithm for crater identification to generate labeled data for NN training can be summarized as follows:

- **Edge detection**: Use the Canny algorithm on the video frames to detect the edges, represented by discrete points, referred to here as edge points (EP)
- **Group the EPs into clusters**: As discussed above, the EPs can be the crater edge or noise. To eliminate the noise, the EPs are grouped into clusters using the following steps:
  - Create a two-dimensional grid over the image with Δx and Δy equal to five times the minimum spacing between the y-sorted EPs
  - Assign each cell of the grid a value equal to the number of EPs lying inside the cell
  - Group the cells into a cluster if the neighboring cells have a non-zero value
- **Identify the cluster with the crater edge**:
  - Check if the EPs in the cluster form a parabolic profile
  - Check if the EPs move a small distance from one frame to another

Figure 3.2(a) and 3.2(b) summarize steps 1 and 2 of the algorithm, and figure 3.2(c) shows the final output of the crater edge by following step 3 of the algorithm.

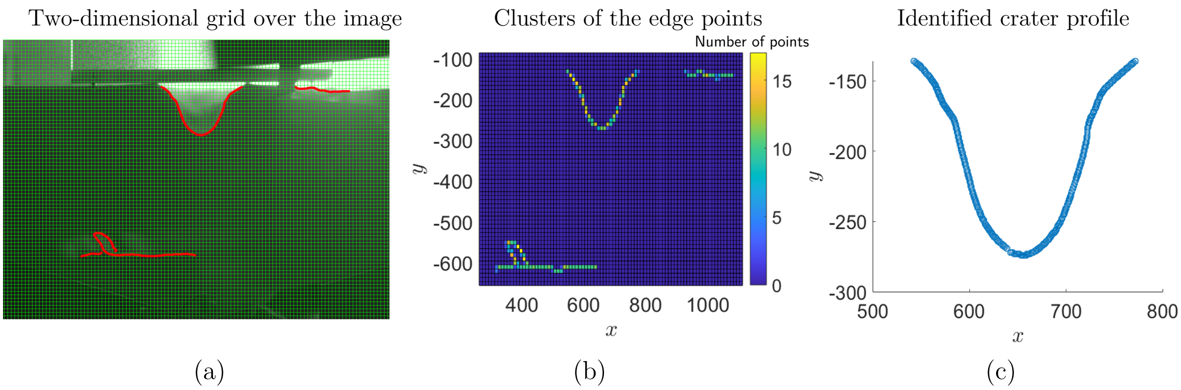

Figure 3.2: Steps in crater identification: (a) a two-dimensional grid over the video frame, (b) binning of the edge points (EPs) and clustering of neighbouring bins, and (c) identified crater profile. Note the axes scales are different in each subfigure.

Labeled data generation using the SAM2 algorithm

The success of the methodology discussed in Section Labeled data generation using the Canny algorithm depends on whether the Canny algorithm detects the entire crater edge (albeit with noise). In practice, however, the output from the Canny algorithm often includes broken edges (see figure 3.1), particularly in cases involving significant ejecta flow within the crater. Therefore, we also evaluate the accuracy of Meta's Segment Anything Model 2 (SAM2) [26] for crater edge detection. SAM2 segments and produces a binary mask of crater and non-crater regions, offering more context for crater edge identification. The advantage with SAM2 is that it allows users to specify positive/negative points or boxes to help identify the region(s) of interest. If the segmentation is inaccurate, the user prompts can correct the mask. Once the mask for the crater is correctly identified in one frame, SAM2 can track it forward/backward in time to identify the crater in all frames.

To improve segmentation of the PFGT1 video frames, background subtraction is performed using the initial frame; the crater mask so generated by SAM2 is shown in figure 3.3(a). This approach works successfully for most cases; however, SAM2 is a pre-trained model and hence sometimes requires additional pre-processing or manual corrections to improve the accuracy of the masks. Therefore, a custom convolutional neural network (CNN) is developed, as discussed in Sections 3.1.2 and 3.1.3, and the crater masks generated by SAM2 are used for CNN training. An in-house trained network provides better control over the performance and opportunities for customizations to enable future tasks, e.g., uncertainty and sensitivity analyses. For edge-based crater identification (discussed in the next section), only the boundary of the mask is required, as shown in figure 3.3(b).

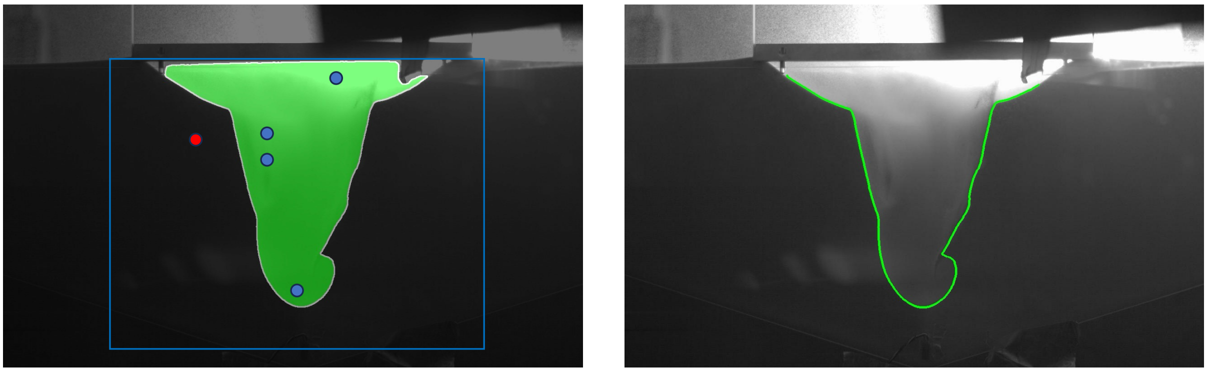

(a) (b)

Figure 3.3: Generating ground truth using SAM2. (a) Crater region mask over the original frame image (blue/red points and box represents positive/negative points and box prompts, respectively). (b) Crater edge obtained after post-processing the crater mask.

This methodology provides labeled training/testing data for the custom CNN model. Data from various cases, listed in Table 3.1, are included for training. These cases span a diverse parameter space (*i.e.*, p_{amb}, $\dot{m}$, and h/d_e values) to include various cratering/ejecta dynamics observed in the videos, *e.g.*, ejecta bursts inside the crater, transitions in crater shape, etc. The diversity of cases in the training data makes the CNN model robust and effective for cases not included in the training data.

Table 3.1: Summary of the labeled dataset for CNN training

Run#	**Regolith**	p_{amb} **(torr)**	h/d_e	$\dot{m}$ **(g/s)**	**No. of labeled images**
R5	MDS	2.003	4	8.6	474
R17	MDS	4.5	10	8.6	463
R19	MDS	0.2	13	0.32	398
R29	MDS	0.02	5	0.32	537
R108	TRI	4.5	3	0.32	496

3.1.2 Edge-based convolutional neural network

Network architecture

Edge detection-based NNs (*e.g.*, [29], [30]) use convolution layers with activation functions to produce the edge/non-edge binary classification of a given image. These applications typically modify an existing classification networks architecture, such as VGG16, AlexNet, etc., by replacing the final classifier layers with up-sampling layers (often called transposed convolution) to produce an output that matches the input dimensions. The feature maps from different convolution layers are up-sampled to produce intermediate outputs, which are subsequently fused together to perform the final pixel-based classification [31]. Sun *et al.* [32] provide a comprehensive review of various edge detection methods using deep learning, such as holistic edge detection (HED), richer convolution features (RCF) network, convolution encoder-decoder networks (CODEC), DeepEdge, etc. Figure 3.4 shows the network architecture used here for edge-based crater identification, adapted from the RCF network [30].

The edge detection NN uses a pre-trained image classification architecture called VGG16 [33], which has multiple stages of convolution layers as a feature extractor. The stage-based architecture allows the network to optimally combine the multi-scale features extracted from various layers for accurate crater identification. At each stage, side outputs of the same size as the ground truth are generated by combining the features from the individual convolution layers and then upsampling these features through transposed convolution layers. The side outputs from each stage are fused to create the final edge prediction. The stage outputs are passed through sigmoid activation, and individual stage loss from stages $s = 1$ to 5 is calculated using the binary cross-entropy with class balance loss function to remove any biases due to a large region of non-edge map compared to a small edge map. (*e.g.*, [29]), given by

$$l^s(A^s_j; W) = -\beta \sum_{j \in Y_+} \log(P(y_j = 0|A^s_j; W)) - (1-\beta) \sum_{j \in Y_-} \log(P(y_j = 1|A^s_j; W)), \quad (3.5)$$

where, $\beta = \dfrac{Y_-}{Y_+ + Y_-}$, $1-\beta = \dfrac{Y_-}{Y_+ + Y_-}$, and Y_+ and Y_- denote the number of pixels representing the edge and non-edge map, respectively. $A^s_j = \{A^s_1, A^s_2, A^s_3, ..., A^s_n\}$ denotes the activation

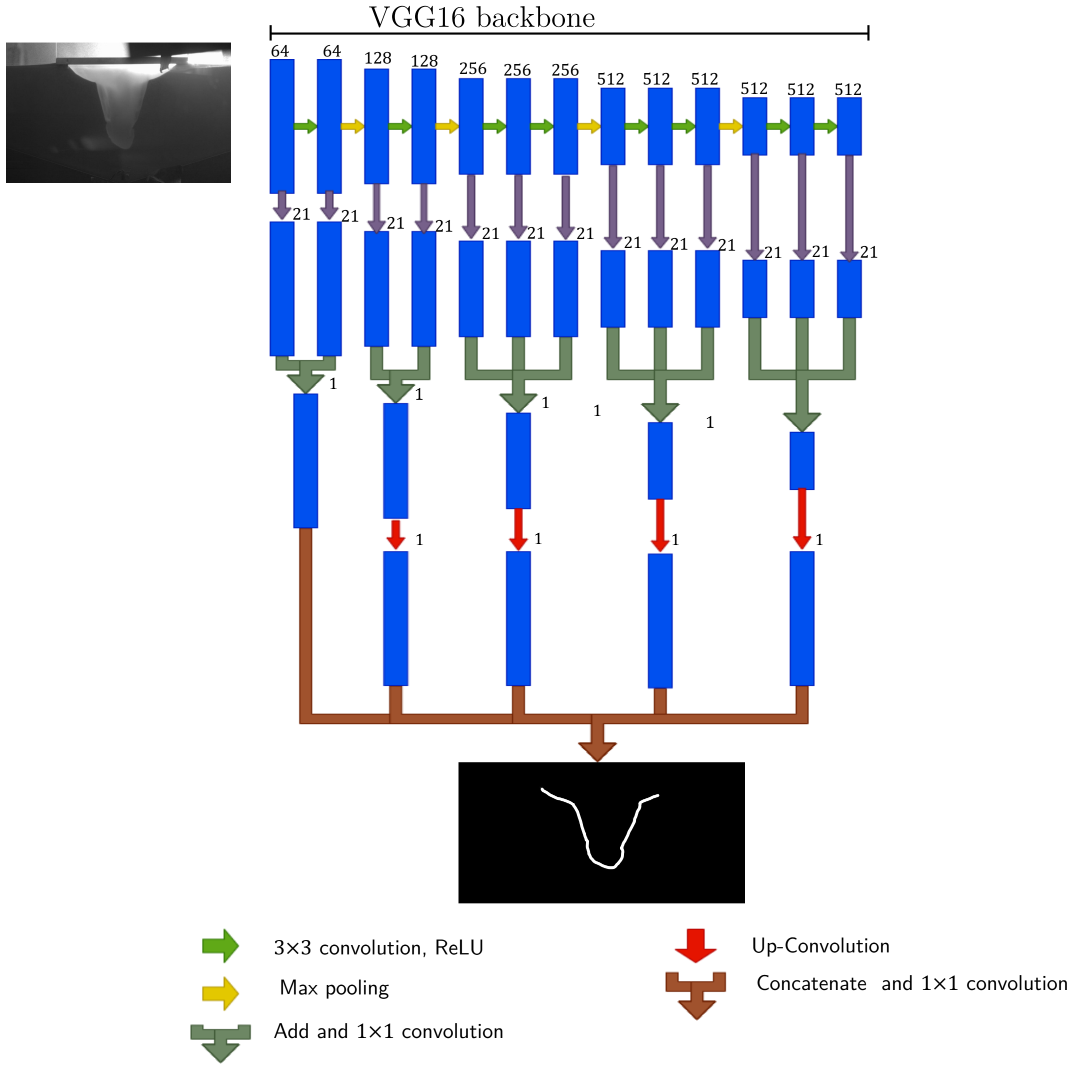

Figure 3.4: Convolution network architecture with pre-trained VGG16 for edge detection.

value and $y = \{y_1, y_2, y_3, ..., y_n\}$ denotes the corresponding binary edge map of ground truth. Also, $P(y_j = 0|A_j^s; W)$ is computed using a sigmoid function where W represents the weights. The total loss is calculated by adding the stage loss and the final prediction loss, $l(A_i^{\text{fuse}}; W)$, which is also calculated using (3.5),

$$L_{\text{total}}(A; W) = \sum_{i=1}^{5} l^s(A_i^s; W) + l^{\text{fuse}}(A_i^{\text{fuse}}; W). \tag{3.6}$$

Training process

A stochastic gradient descent algorithm using momentum with layer-specific learning rates and weight decay parameters to fine-tune different network layers is used as an optimization algorithm to train the network. A learning rate of 10^{-6} and a regularization value of 2×10^{-4} are used as the network's hyperparameters. For effective training, 100 images from each case of the dataset prepared in Section 3.1.1 are used. The remaining images (100 fewer than the number in the last column of Table 3.1 for each case) are used as test images to evaluate the network performance based on the F-measure (*e.g.*, [29])

$$F = \frac{2 \times P \times R}{P + R} \tag{3.7}$$

where, F is the f-score, P is precision and R is the recall. The precision and recall can be calculated by

$$P = \frac{TP}{TP + FP} \tag{3.8}$$

$$R = \frac{TP}{TP + FN} \tag{3.9}$$

where TP (true positive) is the correctly detected edges, FP (False Positive) is the number of non-edges classified as edges, and FN (False Negative) is the number of edges classified as non-edges. Data augmentation, such as horizontal flipping, rotating by 5 different angles $(-5, 5)$, increasing and decreasing contrast by 70-pixel units, and adding random noises on the training images were done before training. This helps to introduce variability in the input images, enabling the network to be trained with fewer training images and reduce overfitting.

3.1.3 Segmentation-based convolutional neural network

Network architecture

Deep learning segmentation architectures, such as fully connected neural networks [31], U-Net [34], etc., have transformed segmentation tasks by learning hierarchical features and accurately identifying regions of interest. Here, a variant of U-Net [34] is used, which has an encoder-decoder structure and is known to perform well for pixel-level classification, e.g., in biomedical imaging. The architecture is illustrated in figure 3.5. The given architecture differs slightly

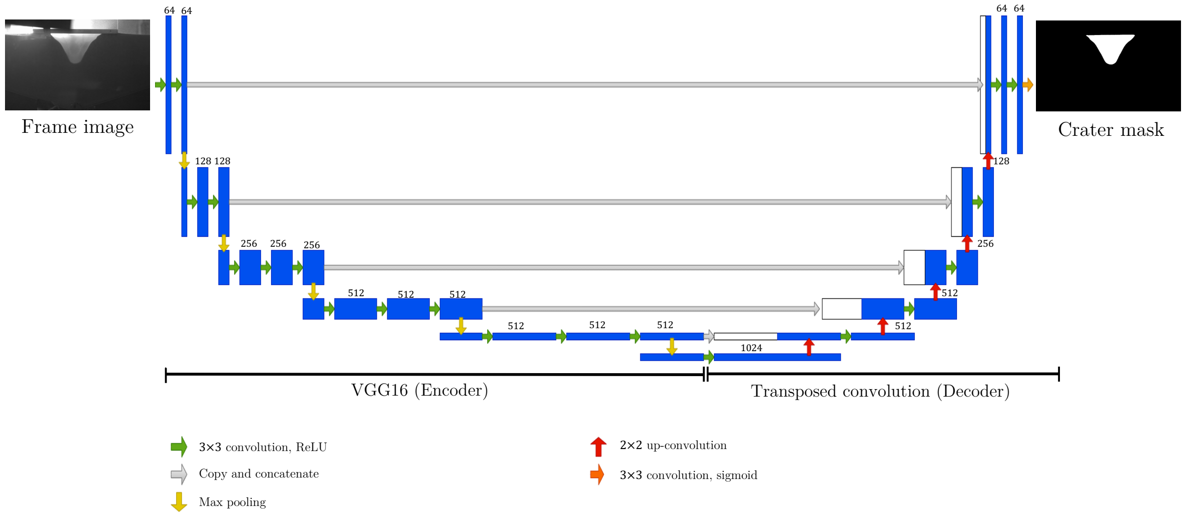

Figure 3.5: UNet architecture with VGG16 as a feature extractor for crater region segmentation.

from the original UNet[34] architecture in the depth of the encoder layer, consisting of 9 convolutional layers, but the overall idea behind the network's operation remains the same. The encoder layer for this network uses a pre-trained VGG16 [33] network with 13 convolutional layers, same as the edge-based network (discussed in Section 3.1.2) to extract the multi-scale features from the input images. Each encoder layer has a corresponding decoder layer that upsamples its input features, which are convolved with a trainable decoder filter to produce a dense feature map. The major differences between this network(figure 3.5) and the edge-based network (figure 3.4) are (i) it has a skip connection from the corresponding encoder to the decoder to combine the high-resolution features from the encoder layer with the upsampled output, and (ii) the decoder is gradually upsampled from the final encoder layer to produce the final prediction. Every layer has ReLU activation except the final layer, which has a sigmoid activation to provide the probabilistic map of the crater and non-crater regions. The binary cross-entropy function given by 3.5 is used to calculate the pixel-wise classification loss between the predicted crater mask and the ground truth. However, for segmentation, binary cross entropy is computed without class balance, so the value of β is substituted as 1 in equation

3.5. Additionally, Dice loss [35] is computed along with a cross-entropy loss to increase the similarity between the network output and ground truth and achieve a perfect overlap between them when the loss approaches zero. It is calculated by

$$L = 1 - D_{\text{coeff}} = 1 - \frac{2\sum_i^N X_i y_i}{\sum_i^N X_i + \sum_i^N y_i} \tag{3.10}$$

where D_{coeff} is the Dice coefficient that measures the similarity between the predicted mask and the ground truth, $X_j = \{X_1, X_2, X_3, ..., X_n\}$ denotes the activation value, and $y = \{y_1, y_2, y_3, ..., y_n\}$ denotes the corresponding binary edge map of ground truth.

Training process

The segmentation-based approach requires each ground truth pixel to be labeled as crater and non-crater regions, producing binary segmentation masks, where 1 represents the crater regions and 0 represents the non-crater regions. SAM2 is leveraged to obtain the crater mask for difficult cases, e.g., those with limited visibility due to ejecta, etc. In addition, the crater profiles obtained by the method described in Section 3.1.1 is used by connecting the ends of the crater profile and filling the inner region with the crater label. 200 images with the corresponding ground truth from each case of Table 3.1 are divided into training/validation sets in the ratio of 9:1. The Adam optimizer [36] is used for training with a learning rate of 10^{-4} and a regularization value of 10^{-8}. The network's performance is evaluated using the Dice coefficient (similar to f-score) given in second part of equation 3.10. Data augmentation, such as horizontal flipping, rotating between -5 and 5 degree, color jittering (increasing and decreasing both brightness and contrast), adding random noise, adding Gaussian blur, and adjusting brightness regionally were introduced during training.

3.2 Convolutional Neural Network (CNN) for crater shape classification

CNNs have been widely used for classifying objects in an image. Various architectures of such networks exist in the literature, *e.g.*, LeNet [37] (MNIST digit classification), AlexNet [38] ,VGG [33] (ImageNet image classification), etc. The core concept behind these architectures is the use of convolutional layers to extract features and classifier layers to identify objects from those extracted features. In this study, this approach is applied to categorize craters by their shape. Instead of classifying the crater directly from images, the classification network uses the output from the segmentation-based (crater identification) network as input. This methodology utilizes the effectiveness of the crater identification network (in generating accurate crater masks) to improve classification accuracy.

3.2.1 Labeled data generation for CNN-based crater shape classification

The crater shapes observed in the PFGT videos can be categorized into: (i) annular,(ii) parabolic, (iii) conical-deep, (iv) conical-annular, and (v) conical-parabolic. For training/testing the network, the crater shapes were manually annotated for 12 different PFGT1 experiment runs (Experiment runs 7 to 18 [24], refer Appendix for the list of experiment runs) that use the MDS regolith. Table 3.2 summarizes the number of frames/images for each crater profile in those runs.

Table 3.2: Summary of the manually annotated crater profiles for training/testing.

Crater shapes	**No. of images**
Parabolic	803
Annular	1387
Conical-annular	1330
Conical-deep	635
Conical-parabolic	1012

3.2.2 Network architecture for crater classification

As discussed above, CNN architecture was used for crater classification, similar to [37], as depicted in figure 3.6. It has two convolution and max pooling layers with ReLU activation to extract the features from the mask. Two fully connected linear layers follow it. Adaptive pooling is used before the classification layer to handle variable-size input images. The final layer computes the probability of each crater class (see Table 3.2) through sigmoid activation. The output is the class with the maximum probability. Categorical cross-entropy, given by 3.11

loss, is calculated to determine the classification loss during training.

$$L_{\text{categorical}} = -\sum_{i=0}^{4} y_i \log(X_i) \tag{3.11}$$

where y_i is the true label (0 or 1 for each class) from the one-hot encoded target vector, and X_i is the predicted probability for class i.

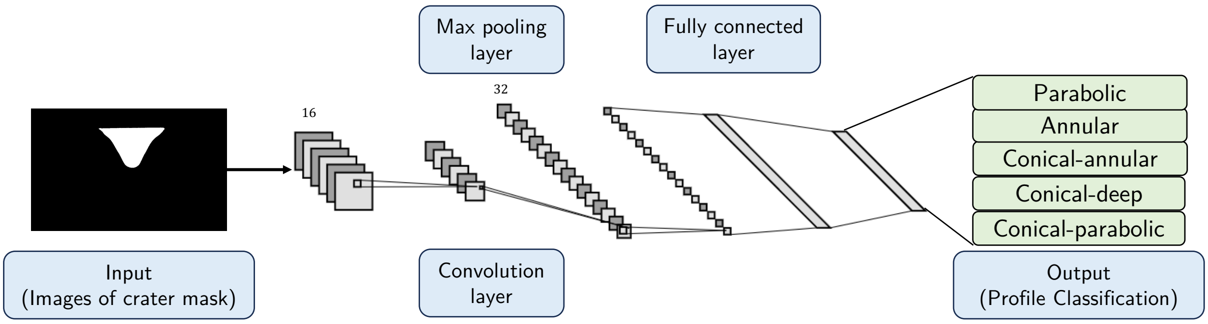

Figure 3.6: Convolutional neural network for crater classification.

Training process

The Adam optimizer is used for optimization with a learning rate of 10^{-3} and a regularization value of 10^{-5}. 200 images from each classified category (given in Table 3.2), making a total of 1000 images, are used for training/validation; 85% for training and 15% for validation. The remaining labeled images (see Table 3.2) were used for testing. During training, the network performance was tracked using training and validation accuracy given by

$$\text{Accuracy} = \frac{\sum_{i=0}^{4} P_i^{+}}{\sum_{i=0}^{4} P_i} \tag{3.12}$$

where P_i^{+} is the correct prediction of each class, and P_i is total prediction of each class. Finally, the trained network is evaluated on the testing set, and a table (called the confusion matrix) is constructed to assess the model's performance in classifying the crater shapes. Data augmentation, such as horizontal flipping, rotating between -15 and 15 degree, translating, and scaling between 0.5 and 1.5 of the image size were introduced during training.

3.3 A data-driven parameteric modeling for crater evolution

Traditional empirical approaches, such as power-law or arctangent fits, etc. have been widely used to approximate crater growth behavior as discussed in Section 1.1.2. However, these relationships often fail to capture the nonlinear transitions and inter operating condition variation as observed in the PFGT data. As described in Section 2.3.2, the crater volume evolves with time; however, the nature of crater evolution depends on parameters such as nozzle height, mass-flow rate, and ambient pressure. Modelling quantities like this is common in fluid flow applications; for example, unsteady aerodynamic loads may vary with mach number and geometric details.

A common solution to modeling operating-parameter-dependent temporal response is to construct a representation in which the response is expressed as a combination of a time-dependent function and an operating-parameter-dependent function within a single, unified model. Therefore, the volume evolution is separated into a temporal response and its dependence on operating conditions. These temporal and parameter responses can be represented as a Fourier basis of sine or cosine curves, spline curves, or a simple polynomial basis. In this thesis, the polynomial representation of temporal evolution, with the parametric dependence modeled by the polynomial coefficients, is formulated. Since the exact relationship between this coefficient and operating conditions is unknown, and the data are sparse across these conditions, a single-parameter polynomial model is employed. In a single-parameter model, the coefficient is a function of a single operating parameter, such as ambient pressure, nozzle height, or mass flow rate.

3.3.1 Labelled data generation for training and testing model for crater evolution

The polynomial based parametric model was trained using crater evolution data obtained from the experiment, as described in Section 2.3.2. The temporal evolution of crater geometry was extracted from each experiment run under varying operating conditions, including nozzle height above the surface ($\bar{h}/\bar{d}_{\mathrm{e}}$), mass-flow rate ($\bar{\dot{m}}$), and ambient pressure ($\bar{p}_{\mathrm{amb}}$).

Calibration and extraction of crater geometry

Crater segments extracted from the image processing methodology described in Section 3.1 were initially represented in pixel coordinates. To obtain the corresponding physical dimensions, a geometric calibration was performed using a calibration wedge of known length ($L_{wedge} = 299.72$ mm [39]) that was visible in all recorded frames. The procedure of calibrating a extracted cratering video frame, *e.g.* as shown in Figure 3.7(a) are as follows:

1. A pixel length (L_{px}) of a lower edge was obtained from the image, and the pixel length was divided by the known physical wedge length (L_{wedge}) to determine the pixel to millimeter scale factor, $Spm = L_{\text{px}}/L_{\text{wedge}}$.

2. The inclination of the wedge relative to the image axis was obtained using $\theta = \tan^{-1}\left(\frac{y_2-y_1}{x_2-x_1}\right)$, where (x_1, y_1) and (x_2, y_2) are the lower left and right corners of the wedge. The rotation matrix was constructed as :

$$R(\theta) = \begin{bmatrix} \cos\theta & -\sin\theta \\ \sin\theta & \cos\theta \end{bmatrix}$$

3. The undisturbed sand surface is used as reference to define the origin points, with $x_{po} = (x_1 + x_2)/2$ at the wedge midpoint and $y_{po} = y_{1s} + \left(\frac{y_{2s}-y_{1s}}{x_{2s}-x_{1s}}\right)(x_{po} - x_{1s})$ on the initial bed surface. Here, (x_{1s}, y_{1s}) and (x_{2s}, y_{2s}) are the left and right extremes' coordinates of the sand bed label. These pixel origin points define the physical origin, with $x = 0$ and $y = 0$ at x_{po} and y_{po} respectively.

4. Each crater edge point p was transformed into physical coordinates as

$$p_{\text{mm}} = \frac{1}{S_{pm}}\left(R(\theta)(p - p_{\text{ref}}) - o\right),$$

where p_{ref} is the rotation center (left wedge corner) and $o = (x_{po}, y_{po})$ is the offset to the defined origin.

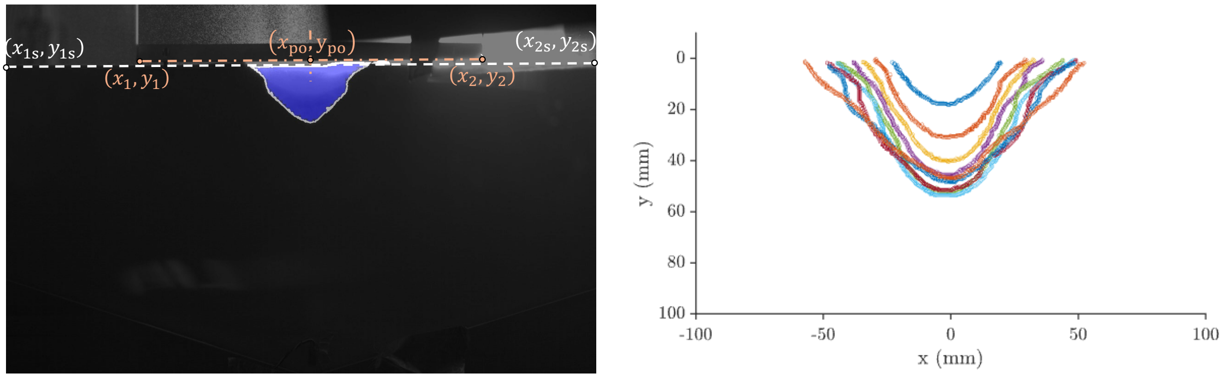

(a) (b)

Figure 3.7: (a) Calibration setup showing different physical points used for calibrating the extracted crater segment (b) Calibrated crater edges at different time snapshots.

Applying the above calibration procedure, the extracted crater geometries from the PFGT videos were expressed in consistent physical units as illustrated in Figure 3.7(b). Depth (H) was calculated as the distance from the surface to the minimum points in the crater. Diameter (D) was calculated as the distance between the two extreme points of the crater profiles. Volume (V) was calculated with axisymmetric assumptions to provide an estimate of the volume of the crater. To remove noise during extraction, an Octave filter [40, 41] was used to smooth the random irregularities in the evolution graph. In this way, the evolution of the crater over time (*e.g.* crater volume evolution) was obtained as shown in Figure 2.4.

3.3.2 Polynomial feature map for coefficient determination

The temporal evolution of volume is modeled with a polynomial function by applying a feature map that projects time into a degree-d monomial basis,

$$\phi(t) = [t^0, t^1, \ldots, t^d]^\top. \tag{3.13}$$

In the feature map, the inputs are transformed into family of monomial functions. The resulting expression for crater volume is

$$V(t) = \mathbf{C}^\top \phi(t), \tag{3.14}$$

where $\mathbf{C}$ denotes the vector of polynomial coefficients associated with a given operating condition. The feature map consists of neuron of monomials as given in Figure 3.8. The polynomial

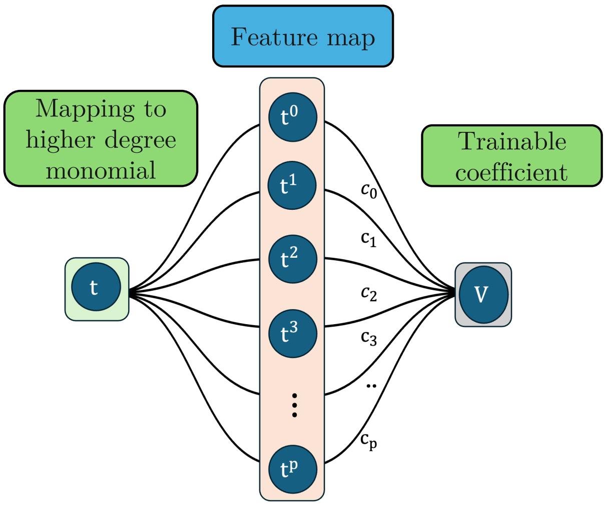

Figure 3.8: Representation of polynomial feature map as a family of monomial basis functions.

representation offers a unified functional form for all crater evolution curves and enables analytical examination of the temporal dynamics using quantities derived directly from the coefficient vector $\mathbf{C}$. Before expressing the coefficient vector as $\mathbf{C} = f(\dot{m}, h/d_e, p_{amb})$, the inherent temporal complexity of the cratering process across varying operating conditions was evaluated. To ensure that the selected polynomial degree captures only the shape of the temporal evolution, and not its absolute scale, time and crater volume are normalized to the ranges $[-1, 1]$ and $[0, 1]$, respectively, for each case.

To characterize the complexity of crater evolution, the curvature of the temporal evolution using the fitted polynomial feature map is quantified as,

$$\|V''\|_{L_2} = \left(\sum_{i=1}^{N_t} \left| \frac{d^2}{dt^2} \mathbf{C}^\top \phi(t_i) \right|^2 \Delta t \right)^{1/2} . \tag{3.15}$$

which serves as a measure of the degree of nonlinearity during crater growth. Small curvature values correspond to smooth evolution dominated by a single growth regime, whereas larger curvature values indicate the presence of inflection points, rapid variations in erosion rate, or multiple distinct temporal phases. In addition, we characterize the maximum instantaneous rate of volume change through a temporal Lipschitz constant defined as

$$\mathcal{L} = \max_{1 \leq i \leq N_t} \left| \frac{d}{dt} \mathbf{C}^\top \phi(t_i) \right|. \tag{3.16}$$

which captures the steepest rate of change in volume over time. Higher values correspond to sudden cratering events or sharp transitions in crater development, while lower values reflect more gradual, continuous evolution. Degree obtained from the feature map is defined to be an effective degree (d_{eff}) of polynomial fit, if L_2 error given by Eq. 3.17 is less than 0.01.

$$L_2 \,\text{error} = \frac{\left(\sum_{i=1}^{N_t} \left(\hat{V}(t_i) - V(t_i) \right)^2 \right)^{1/2}}{\left(\sum_{i=1}^{N_t} V(t_i)^2 \right)^{1/2}}. \tag{3.17}$$

Here, N_t is volume time points used for training, and V and $\hat{V}$ are the actual and predicted volumes of the crater.

Single-parameter coefficient models

Single-parameter coefficient models are constructed with the polynomial feature map (described in Section 3.3.2) in each operating parameter. These models show how accurately crater-volume evolution can be predicted when only one operating parameter is varied at a time. Since, there is limited number of data across operating parameter, *e.g.*, there are only three pressure values when mass flow rate and ambient pressure are fixed as discussed in Section 2.3.2, it limits the training and testing of the model. However, the proposed single parameter model is robust and can be improved with inclusion of more data.

Single parameter modeling for each operating parameter slice (discussed in Section 2.3.2) was performed on the temporal volume evolution. For each operating condition, the crater volume evolution is expressed using a fixed 6 degree polynomial feature map in normalized time ($t \in [-1, 1]$) given in Eq. 3.14 where $\mathbf{C}$ is the coefficient vector associated with one operating parameter. Thus, the coefficient obtained from the polynomial fitting carries the information of scaling with the operating parameter. In the single-parameter baseline, the coefficient vector is modeled as a function of a single operating parameter ($\beta = h/d_{\mathrm{e}}$, p_{amb}, or $\dot{m}$). Each coefficient is assumed to vary smoothly with β and is approximated using a low-order polynomial,

$$C_k(\beta) = \sum_{s=0}^{S} c_{k,s}\, \beta^s, \qquad s = 0, \ldots, S. \tag{3.18}$$

Substituting Eq. 5.1 into Eq. 3.14 yields the explicit baseline predictor

$$\hat{V}(t;\beta) = \sum_{k=0}^{d} \left(\sum_{s=0}^{S} c_{k,s}\, \beta^s \right) t^k, \tag{3.19}$$

which preserves a fixed temporal basis while allowing parameter-dependent variability through the coefficient vector.

The performance of the single-parameter model is evaluated using leave-one-out (LOO) cross-validation, which is particularly suitable for data-scarce regimes[42]. This validation method helps to identify the critical operating parameters required for accurate modeling. For each parameter vector, one operating condition is excluded (held-out), the coefficient mappings $C_p(x)$ are fitted using the remaining cases, and Eq. 5.2 is used to reconstruct the full time history of the held-out case. The coefficient–parameter degree r in each single-parameter slice is chosen based on the identifiability under leave-one-out (LOO) fitting and a bias–variance trade-off. In a slice with N_x distinct operating conditions, LOO leaves $N_x - 1$ training points; fitting a degree-r polynomial for each coefficient requires at least $r + 1$ training points, hence $r \leq N_x - 2$. This drives the minimum degree fitting that we did for the individual model. Since time is normalized to [-1, 1] per operating conditions, an exact mapping to physical time must be known before accurately reconstructing the temporal volume evolution. Prediction accuracy is quantified using the relative L_2 error over the entire temporal evolution.

Chapter 4

Evaluation of Convolutional Neural Network (CNN) for crater geometry extraction and classification

4.1 Edge-based and segmentation-based crater geometry identification

The edge-based network is trained for 15 epochs on the augmented training images, as discussed in Section 3.1.2. The F-score, equation (3.7), for the trained network is 0.93 on the testing images. Similarly, the segmentation-based network is trained for 60 epochs on the training images, as described in Section 3.1.3, and yielded a Dice coeficient of 0.963 on the validation set and 0.9 on the testing images.

To evaluate the NN performance, the PFGT videos are categorized into Easy, Moderate, Challenging, and Extreme, based on the level of difficulty in crater edge identification. The difficulty level, as elaborated in Table 4.1, is assigned from the degree of ejecta flow, sand adhesion to the splitter plate, brightness variations, etc., which obscure the crater view, and our experience with crater identification using the Canny algorithm and SAM2 (discussed in Section 3.1.1). The challenging and extreme cases represent runs with high mass flow rate ($\dot{m}$), low nozzle height (h/d_e), or a combination of both. The (edge-based and segmentation-based) network performance is assessed by their accuracy in detecting the crater edge or mask for various runs. For discussion, we use four performance categories: (i) Excellent, (ii) Good, (iii) Fair, and (iv) Poor. The differences in the definitions of those categories for each network are outlined in Table 4.2.

Figure 4.1 shows an example of the results from both (edge-based and segmentation-based) networks on frames of various difficulty levels. As evident, both networks perform well for the Easy frame (Perfect prediction). In the Moderate difficulty frame, the edge-based

Table 4.1: Description of various difficulty levels.

Difficulty levels	Description	No. of cases
Easy	Clear visibility, smooth transitions, and minimal ejecta flow	22
Moderate	Smoky view, brightness variations across the frames, sand adhesion to the splitter plate, and moderate ejecta flow	13
Challenging	Streaks of ejecta within the crater, quick crater geometry transitions with strong ejecta flow, and the presence of nozzle in the frame	15
Extreme	Poor visibility due to excessive ejecta flow within and outside the crater, dark crater blending with the bed material, and crater imprints on the acrylic pane from previous runs	5

Table 4.2: Description of various performance categories.

Performance Categories	Edge-Based Detection Details	Segmentation-Based Detection Details
Excellent	Perfectly detects the crater edge.	Perfectly detects the crater region mask.
Good	Detects the crater edges along with some irrelevant edges.	Detects the crater region with minimal extraneous regions outside the crater.
Fair	Detects a discontinuous edge profile within the crater and other irrelevant edges.	Detects incomplete crater region mask that may be misaligned.
Poor	Detects little to no part of the crater; extreme failure in edge detection.	Detects only a small portion of the crater region or fails completely.

approach generates some outliers (Good prediction), while the segmentation approach is perfect. In the Challenging frame, the edge-based method produces discontinuous edges (Fair prediction), whereas the segmentation approach is again perfect, generating an accurate mask of the crater. In the Extreme case, the edge-based prediction fails to produce the complete (crater) edge, missing most of the geometrical information, such as the height and width of the crater (Poor prediction). On the other hand, the segmentation method captures a significant portion of the crater, estimating its height and width reasonably accurately (Fair prediction).

To quantitatively compare the performance of edge and segmentation-based networks, Table 4.3 provides the percentage of images at each difficulty level with Excellent, Good, Fair, and Poor predictions. Such tables are typically referred to in the machine learning community

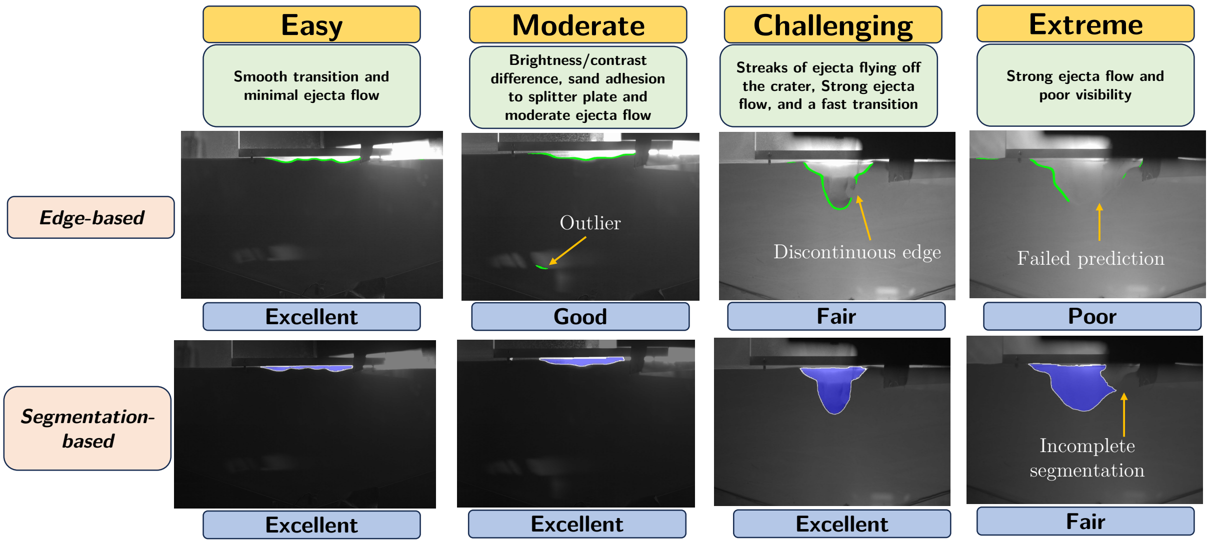

Figure 4.1: Edge-based and segmentation-based predictions with the corresponding performance category at different difficulty levels.

Table 4.3: Confusion matrix illustrating the prediction performance based on the difficulty levels.

Difficulty levels	Edge-based (%)				segmentation-based (%)			
	Excellent	Good	Fair	Poor	Excellent	Good	Fair	Poor
Easy	54.5	27.3	18.2	0.0	59.1	27.3	13.6	0.0
Moderate	46.2	46.2	0.0	7.7	61.5	30.8	0.0	7.7
Challenging	6.7	13.3	80.0	0.0	53.3	26.7	20.0	0.0
Total(%)	33.9	25.0	32.1	8.9	51.8	26.8	17.9	3.6

as the confusion matrix [43]. Excellent and Good results can be considered a success for the NN since they imply the crater profile is accurately captured. For Easy and Moderate difficulty frames, both the edge and segmentation-based networks perform reasonably well. In Challenging cases, the segmentation-based prediction produces 80.0% Excellent and Good results, outperforming the edge-based prediction, which yields only 20.0% Excellent and Good results. In Extreme cases, both models struggle; however, the segmentation-based method has 80% Fair results, compared to only 20% with the edge-based approach. Moreover, a Fair prediction with segmentation-based NN provides some geometric information, while a Fair result with edge-based detection implies discontinuous edges, losing most of the crater geometric information. Based on these observations, the segmentation-based NN is superior to the edge-based NN.

4.2 Crater shape classification

The crater classification network (see Section 3.2.2) leverages the output (binary representation of crater and non-crater region) of the segmentation-based network (see Section 3.1.3) as input and classifies the corresponding crater shape. The success of the classifier is dependent on the segmentation-based NN's better performance (see Section 4.1 for the results). Thus, the classifier network can only predict the crater shape for the valid segmented crater regions from the frame. It is trained for 20 epochs on the training and validation datasets (see Section 3.2.1 and 3.2.2). Figure 4.2(a) shows the learning curve during training. The performance evaluation of the network on the testing data yields an accuracy of 97.58%. The confusion matrix, see figure 4.2(b), illustrates that the classification accuracy for each crater shape is high. The conical-deep profile's classification has the highest accuracy of 100%, while the parabolic profile classification has the lowest accuracy of 94.88% among all shapes. Around 2.81% of parabolic profiles are misclassified as conical deep. Similarly, 2.38% of the conical-annular profile is falsely categorized as parabolic.

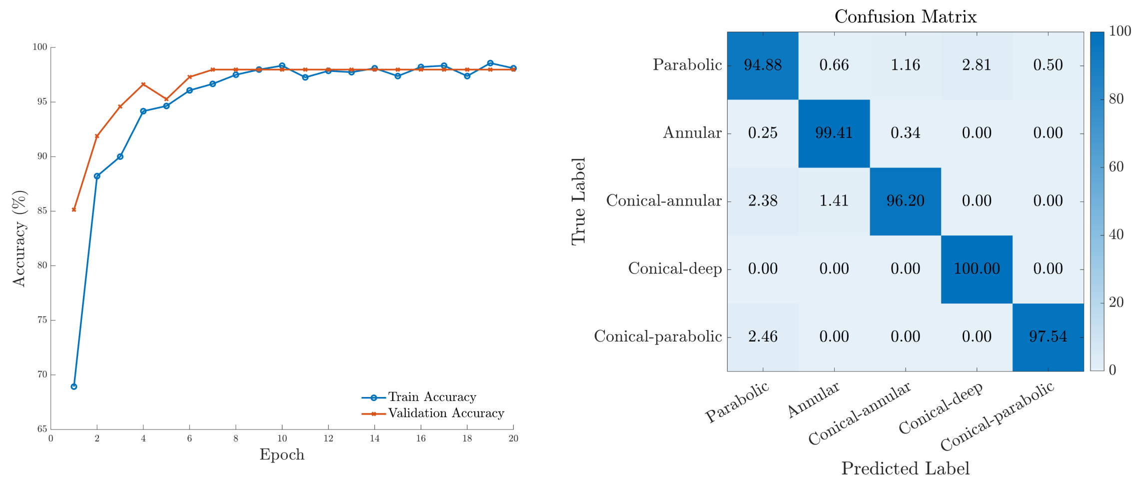

(a) (b)

Figure 4.2: (a) Learning curve during training (b) Confusion matrix of test data in percent score.

Furthermore, the trained classifier's performance is assessed qualitatively by predictions for cases that were not included in the training and testing dataset. Figure 4.3 shows different

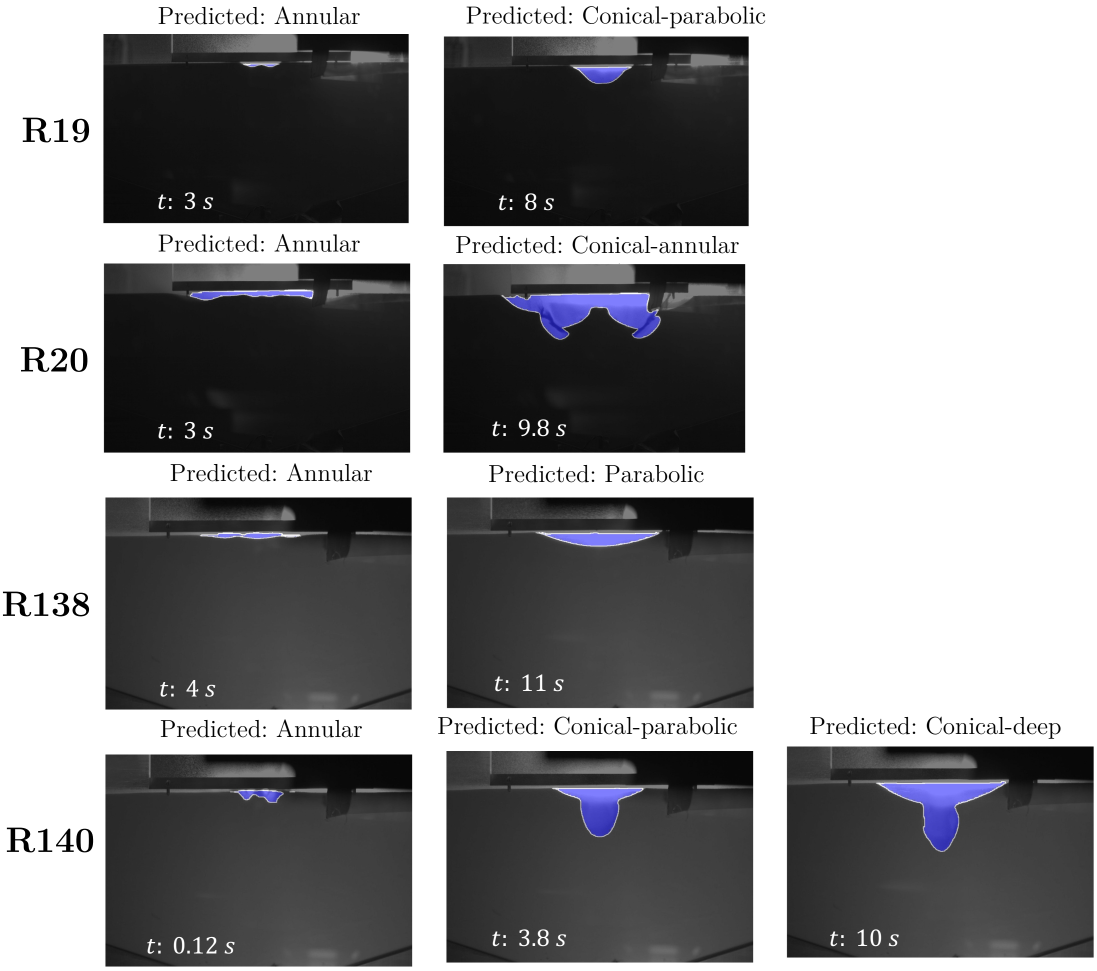

Figure 4.3: Crater geometry classification for various experimental runs (not part of the training data).

crater shapes predicted by the trained classifier network. It can accurately predict the crater geometry in the experimental runs that were excluded from the training data.

Chapter 5

Evaluation of data-driven parameteric modeling for crater evolution

5.1 Fitting polynomial feature maps through temporal volume evolution

The numerical values of the effective polynomial degree (d_{eff}), curvature $\|V''\|_{L_2}$, and Lipschitz constant $\mathcal{L}$ for representative cases are summarized in Table 5.1 and the polynomial fit for all operating conditions are given in the Appendix B. The table confirms that all three metrics vary systematically with the operating conditions and changes precisely in regimes where crater-shape transitions occur, as documented in Section 2.3.2. In every parameter slice, cases with higher d_{eff} also exhibit larger curvature and larger $\mathcal{L}$, indicating both greater temporal nonlinearity and increased sensitivity to operating parameters. The effective polynomial degree alone indicates the minimum functional complexity required to represent the temporal evolution, but it does not distinguish between gradual nonlinear growth and abrupt changes in cratering. The curvature norm $\|V''\|_{L_2}$ provides a measure of how strongly the evolution departs from linear or weakly nonlinear behavior, while the maximum temporal rate $\mathcal{L}$ quantifies the steepest instantaneous crater volume growth. Together, these metrics enable discrimination between smoothly evolving regimes and transitional regimes characterized by sharp temporal changes.

(i) Fixed mass flow rate and nozzle height ($\bar{\dot{m}} = 0.32$ g/s, $\bar{h}/\bar{d}_{\text{e}} = 10$). When ambient pressure varies, Table 5.1 indicates that d_{eff} increases at low pressures where a conical component emerges, along with moderate increases in curvature and $\mathcal{L}$. At intermediate pressure $\bar{p}_{\text{amb}} = 2$ torr, both curvature and maximum temporal rate are the highest as the crater volume is transitioning to asymptotic behavior in the time interval. At higher pressures $\bar{p}_{\text{amb}} = 4.5$ torr,

Table 5.1: Effective polynomial degree d_{eff}, curvature norm $\|V''\|_{L_2}$, and maximum temporal rate (Lipschitz constant) $\mathcal{L}$ for representative cases.

Operating condition	d_{eff}	$\|V''\|_{L_2}$	$\mathcal{L}$
$\bar{\dot{m}} = 0.32$ g/s, $\bar{h}/\bar{d}_{\text{e}} = 10$			
$\bar{p}_{\text{amb}} = 0.02$ torr	5	1.070	0.821
$\bar{p}_{\text{amb}} = 2$ torr	5	1.739	0.992
$\bar{p}_{\text{amb}} = 4.5$ torr	3	0.481	0.653
$\bar{\dot{m}} = 0.32$ g/s, $\bar{p}_{\text{amb}} = 0.02$ torr			
$\bar{h}/\bar{d}_{\text{e}} = 5$	4	1.777	0.907
$\bar{h}/\bar{d}_{\text{e}} = 6$	4	1.403	0.809
$\bar{h}/\bar{d}_{\text{e}} = 8$	4	0.979	0.773
$\bar{h}/\bar{d}_{\text{e}} = 10$	5	1.070	0.821
$\bar{h}/\bar{d}_{\text{e}} = 13$	3	1.011	0.700
$\bar{p}_{\text{amb}} = 4.5$ torr, $\bar{h}/\bar{d}_{\text{e}} = 10$			
$\bar{\dot{m}} = 0.32$ g/s	3	0.481	0.653
$\bar{\dot{m}} = 8.6$ g/s	6	2.208	0.918

the temporal evolution becomes smoother and all three metrics decrease, consistent with the weakening of the conical–parabolic transition.

(ii) Fixed mass flow rate and ambient pressure ($\bar{\dot{m}} = 0.32$ g/s, $\bar{p}_{\text{amb}} = 0.02$ torr). When nozzle height varies, Table 5.1 shows that d_{eff} increases from 4 at low heights to 5 at intermediate heights ($\bar{h}/\bar{d}_{\text{e}} = 10$), coinciding with annular-to-parabolic and parabolic-to-annular transitions. At lower $\bar{h}/\bar{d}_{\text{e}} = 5$–$6$, the curvature of the temporal volume evolution is higher than the rest, indicating a more complex annular-to-parabolic transition. At intermediate and higher heights, all three metrics decrease again, consistent with a return to a smoother annular regime.

(iii) Fixed ambient pressure and nozzle height ($\bar{p}_{\text{amb}} = 4.5$ torr, $\bar{h}/\bar{d}_{\text{e}} = 10$). When the mass flow rate varies, the most pronounced changes are observed. Table 5.1 shows that low–mass-flow ($\bar{\dot{m}} = 8.6$ g/s) case requires $d_{\text{eff}} = 3$ with relatively small curvature (0.481) and $\mathcal{L} = 0.653$, whereas high–mass-flow ($\bar{\dot{m}} = 8.6$ g/s) case requires $d_{\text{eff}} = 6$ and exhibit the largest curvature (2.208) and $\mathcal{L} = 0.918$ in the dataset, indicating complex temporal transition. These increases may be due to the onset of parabolic to conical-deep transitions.

Overall, Table 5.1 indicates that the effective polynomial degree, curvature, and maximum temporal rate (Lipschitz constant) together provide a consistent set of diagnostics. All three vary markedly at the same operating conditions where crater-shape transitions arise, yielding a compact, quantitative description of the temporal complexity of crater evolution.

Fitting a polynomial with effective degree reflects crater-evolution physics but produces coefficient vectors of varying length, so coefficients lose a consistent physical meaning and cannot serve as stable machine-learning targets. Sparse sampling worsens this by causing jumps in polynomial degree and coefficient dimension. The next sub sections, therefore, adopt a fixed-degree polynomial basis, keeping enough flexibility while enforcing a fixed-size coefficient vector with uniform interpretation across single operating parameter to model crater volume evolution.

5.2 Single-parameter coefficient models based on a polynomial feature map

Single parameter modeling for each operating parameter slice (discussed in Section 2.3.2) was performed on the temporal volume evolution. For each operating condition, the crater volume evolution is expressed using a fixed 6 degree polynomial feature map in normalized time ($t \in [-1, 1]$) given in Eq. 3.14 where $\mathbf{C}$ is the coefficient vector associated with one operating parameter. A 6 degree polynomial is selected because the effective-degree analysis in Section 5.1 shows that all observed crater evolution curves $d_{\text{eff}} \leq 6$ is enough to represent them as polynomial function. Thus, the coefficient obtained from the polynomial fitting carries the information of scaling with the operating parameter. In the single-parameter baseline, the coefficient vector is modeled as a function of a single operating parameter (non-dimensional $\beta = h/d_e$, p_{amb}, or $\dot{m}$). Each coefficient is assumed to vary smoothly with x and is approximated using a low-order polynomial,

$$c_k(\beta) = \sum_{s=0}^{S} c_{k,s}\,\beta^s, \qquad s = 0, \ldots, S. \tag{5.1}$$

Substituting Eq. 5.1 into Eq. 3.14 yields the explicit baseline predictor

$$\hat{V}(t;\beta) = \sum_{k=0}^{d} \left(\sum_{s=0}^{S} c_{k,s}\,\beta^s \right) t^k, \tag{5.2}$$

which preserves a fixed temporal basis while allowing parameter-dependent variability through the coefficient vector.

The performance of the single-parameter model is evaluated using leave-one-out (LOO) cross-validation, which is particularly suitable for data-scarce regimes[42]. This validation method helps to identify the critical operating parameters required for accurate modeling. For each parameter vector, one operating condition is excluded (held-out), the coefficient mappings $C_p(x)$ are fitted using the remaining cases, and Eq. 5.2 is used to reconstruct the full time history of the held-out case. The coefficient–parameter degree r in each single-parameter slice is chosen based on the identifiability under leave-one-out (LOO) fitting and a bias–variance trade-off. In a slice with N_x distinct operating conditions, LOO leaves $N_x - 1$ training points; fitting a degree-r polynomial for each coefficient requires at least $r + 1$ training points, hence $r \leq N_x - 2$. This drives the minimum degree fitting that we did for the individual model. Since time is normalized to [-1, 1] per operating conditions, an exact mapping to physical time must be known before accurately reconstructing the temporal volume evolution. Prediction accuracy is quantified using the relative L_2 error over the entire temporal evolution.

Fixed mass flow rate and height

For the pressure slice $\bar{p}_{\mathrm{amb}} = [0.02, 2, 4.5]$ torr, fixed $\bar{\dot{m}} = 0.32$ g/s and $\bar{h}/\bar{d}_{\mathrm{e}} = 10$ (as discussed in section 2.3.2) a linear coefficient model ($r = 1$) is employed,

$$\hat{V}(t; p_{amb}) = \sum_{k=0}^{6} (c_{k,0} + c_{k,1} p_{amb})\, t^k. \tag{5.3}$$

Coefficients for the linear model representing varying ambient pressure is given in the Appendix (Table B.1). Figure 5.1(a) shows the L2 error in LOO cross-validation. Across the three ambient pressures, the baseline yields relative L_2 errors of $\mathcal{O}(0.3–0.5)$. Errors are maximum when the minimum(($\bar{p}_{\mathrm{amb}} = 0.02$ torr)) and maximum ($\bar{p}_{\mathrm{amb}} = 4.5$ torr) pressures are held-out, inferring worse performance in extrapolation. Error for intermediate presure ($\bar{p}_{\mathrm{amb}} = 2$ torr) is distributed throughout the temporal evolution as shown in Figure 5.1(b), indicating that linear interpolation of coefficients in $\bar{p}_{\mathrm{amb}}$ alone does not adequately capture pressure-driven

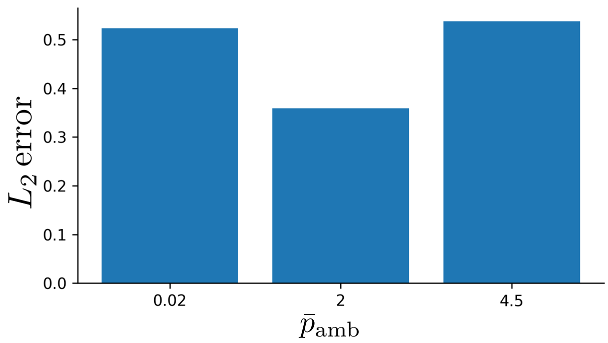

(a)

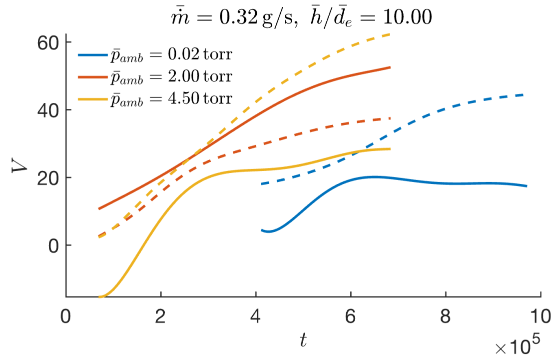

(b)

Figure 5.1: (a) L_2 error bar plot of leave-one-out cross validation for $\bar{p}_{\mathrm{amb}}$ (b) Prediction of volume evolution on held-out $\bar{p}_{\mathrm{amb}}$ using single parameter coeficient models fitted on remaining $\bar{p}_{\mathrm{amb}}$ and fixed $\bar{\dot{m}} = 0.32$ g/s and $\bar{h}/\bar{d}_{\mathrm{e}} = 10$. Dashed lines (- -) represent the experimental crater volume, while solid lines (–) represent the predicted volume.

changes in crater evolution. This implies having more ambient pressure data to fit a higher degree polynomial through pressure for accurate reconstruction.

Fixed mass flow rate and ambient pressure

For $\bar{h}/\bar{d}_{\mathrm{e}} = [5, 6, 8, 10, 13]$ and fixed $\bar{\dot{m}} = 0.32$ g/s and $\bar{p}_{\mathrm{amb}} = 0.02$ torr, a quadratic coefficient for $\bar{h}/\bar{d}_{\mathrm{e}}$ ($r = 2$) is fitted yield volume evolution as,

$$\hat{V}(t; h/d_{\mathrm{e}}) = \sum_{k=0}^{6} \left(c_{k,0} + c_{k,1}(h/d_{\mathrm{e}}) + c_{k,2}(h/d_{\mathrm{e}})^2\right) t^k. \tag{5.4}$$

Coefficients for the the quadratic model obtained by fitting a polynomial feature map for varying $\bar{h}/\bar{d}_{\mathrm{e}}$ is given in Appendix (Table B.2). LOO result in Figure 5.2(a) shows that the prediction accuracy is highest at intermediate heights (e.g. $\bar{h}/\bar{d}_{\mathrm{e}} = 10$, $L_2 \approx 0.045$) and degrades sharply at lower heights ($\bar{h}/\bar{d}_{\mathrm{e}} = 5$–$6$, $L_2 \approx 0.54$–0.73), which correspond to annular–parabolic transition regimes. Figure 5.2(b) shows that volume evolution significantly shifted in these transitional regime. This behavior indicates that smooth, low-order coefficient interpolation in $\bar{h}/\bar{d}_{\mathrm{e}}$ fails when crater evolution changes rapidly with nozzle height. More $\bar{h}/\bar{d}_{\mathrm{e}}$ in the transition regime (between $\bar{h}/\bar{d}_{\mathrm{e}} = 6 - 8$), might improve the performance of the height model.

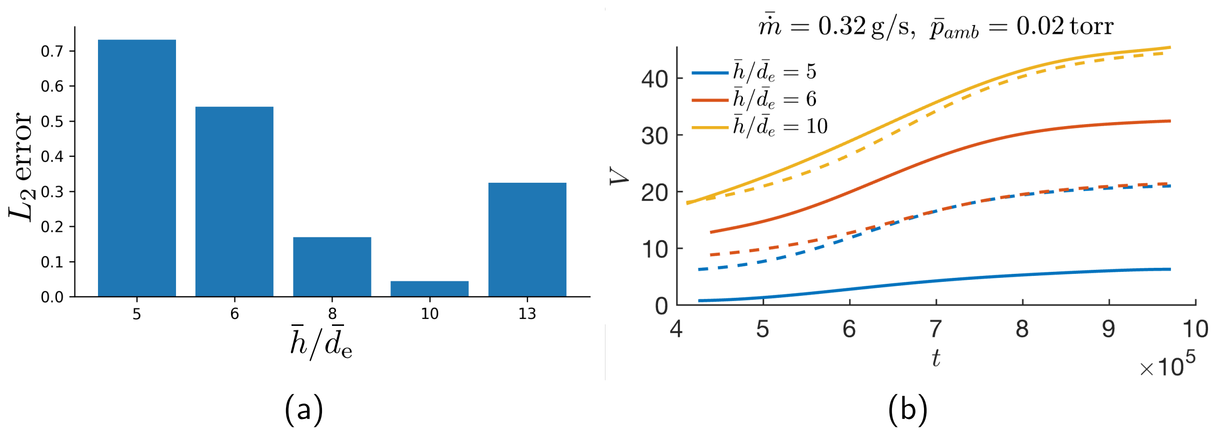

Figure 5.2: (a) L_2 error bar plot of leave-one-out cross validation for $\bar{h}/\bar{d}_\mathrm{e}$(b) Prediction of volume evolution on held-out $\bar{h}/\bar{d}_\mathrm{e}$ using single parameter coefficient models fitted on remaining $\bar{h}/\bar{d}_\mathrm{e}$ and fixed $\bar{\dot{m}} = 0.32$ g/s and $\bar{p}_\mathrm{amb} = 0.02$ torr. Dashed lines (- -) represent the experimental crater volume, while solid lines (–) represent the predicted volume.

Fixed height and ambient pressure

Only two distinct mass-flow rate $\bar{\dot{m}} = 0.32$ g/s and $\bar{\dot{m}} = 8.6$ g/s are available for fixed $\bar{p}_\mathrm{amb} = 4.5$ torr and $\bar{h}/\bar{d}_\mathrm{e} = 10$. Under LOO cross-validation, the training set collapses to a single point, forcing the coefficient mapping to reduce to a constant ($r = 0$),

$$\hat{V}(t;\dot{m}) \equiv \sum_{k=0}^{6} c_{k,0}\, t^k. \tag{5.5}$$

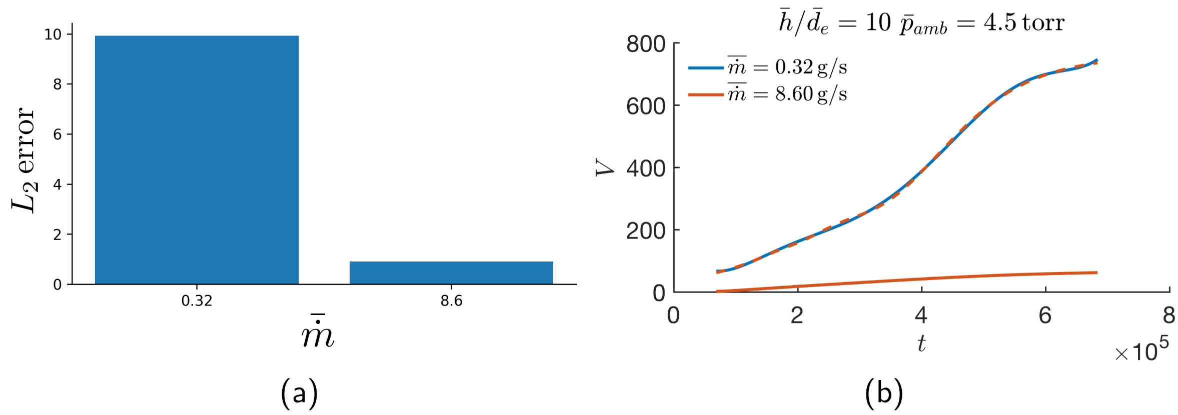

Figure 5.3: (a) L_2 error bar plot of leave-one-out cross validation for $\bar{\dot{m}}$ (b) Prediction of volume evolution on held-out $\bar{\dot{m}}$ using single parameter coefficient models fitted on remaining $\bar{\dot{m}}$ and fixed $\bar{h}/\bar{d}_\mathrm{e} = 10$ and $\bar{p}_\mathrm{amb} = 4.5$ torr. Dashed lines (- -) represent the experimental crater volume, while solid lines (–) represent the predicted volume.

Consequently, the predictions are nearly identical for different values of $\bar{\dot{m}}$, as shown in Figure 5.3(b), because each leave-one-out prediction relies on a single coefficient model fitted to the volume evolution. Large errors ($L_2 \gtrsim 0.9$) indicate a poorly performing coefficient model, which arises from having only two mass flow rate operating conditions. This case explicitly illustrates the impact of insufficient intermediate data on inference. Appendix B.3 reports a linear model, rather than a constant model, for mass, in which the two mass flow rates are fitted. However, the prediction accuracy of the volume evolution in the intermediate range $\bar{\dot{m}} = 0.32$-8.6 g/s cannot be quantified with only these two operating conditions. At least one additional mass flow rate is required to validate the model.

Chapter 6

Conclusions and future work

The underlying physics governing erosion mechanisms in PSI can be investigated by examining crater evolution. This study utilizes high-speed videos from subscale PSI experiments at reduced pressures (and various nozzle heights, mass flow rates, and regoliths) to extract and classify the crater geometry. Two deep learning approaches, employing edge and segmentation-based networks, are evaluated to automate the identification of crater geometry from experimental videos. The edge-based network directly determines the crater edge from the video frames, whereas the segmentation-based approach determines a mask for the crater region, which then is post-processed to extract the crater edge. To discuss network performance, the video frames are categorized into four difficulty levels – Easy, Moderate, Challenging, and Extreme – based on crater visibility in the frame, ejecta dynamics, lighting variations, etc., and the performance is categorized into four evaluation criteria, namely, Excellent, Good, Fair, and Poor, depending on the accuracy of predictions and noise. Segmentation-based network produced 51.8% Excellent and 26.8% Good predictions of crater geometry, while the edge-based network produced 33.9% Excellent and 25.0% Good predictions on the Easy, Moderate, and Challenging cases combined. The segmentation-based approach is superior to the edge-based detection for all difficulty levels, although segmenting images with Extreme difficulty remains challenging, producing Fair predictions. The better performance of the segmentation approach over edge detection can be attributed to the fact that the edge-based method detects a very small part of the full image, making it susceptible to information loss.

The study also employed a convolution neural network as a classifier to categorize crater shapes based on the segmentation masks. The categories include parabolic, annular, conical-parabolic, conical-annular, and conical-deep shapes. The trained classifier produced an accuracy of 97.58% on the testing set. Future studies will evaluate the correlation between the classified crater shape/transitions and the erosion mechanism. Broadly, the current work paves the way for creating a response map between the erosion mechanisms and the parameter space (characterizing plume/soil and ambient conditions).

The PSI experiments demonstrate that the crater geometry evolution and transitions are strongly governed by the operating conditions. This thesis evaluated the use of a single parameter coefficient model using polynomial feature map to model crater evolution. By combining U-Net–based image segmentation with geometric calibration, the crater volume data for 21 operating conditions with the MDS soil type was extracted (from the high-speed experimental videos). At fixed $\bar{\dot{m}} = 0.32$ g/s and $\bar{h}/\bar{d}_{\mathrm{e}} = 10$ and varying $\bar{p}_{\mathrm{amb}} = 0.02 - 4.5$ torr, the crater geometry changes from annular to parabolic and conical-parabolic. Similarly, with an increase in height from $\bar{h}/\bar{d}_{\mathrm{e}} = 5$ to 13 at fixed $\bar{\dot{m}} = 0.32$ g/s and $\bar{p}_{\mathrm{amb}} = 0.02$ torr, the crater transforms from parabolic to annular. In addition, the crater exhibits transitions from conical-parabolic to conical-deep with a change in $\bar{\dot{m}}$ from 0.32 g/s to 8.6 g/s at fixed $\bar{p}_{\mathrm{amb}} = 4.5$ torr and $\bar{h}/\bar{d}_{\mathrm{e}} = 10$. These transitions pose difficulties in modeling; therefore, we implemented and analyzed polynomial-based functions rather than existing monomial models (*e.g.,* power-law fits) to model crater volume evolution.

Analysis of polynomial feature maps revealed that the effective polynomial degree, curvature norm, and temporal Lipschitz constant all rise sharply in regions where crater-shape transitions (e.g., from annular to parabolic, parabolic to conical–parabolic, and conical–parabolic to conical–deep, etc.). In smoothly varying regimes, low-degree polynomials ($d_{\mathrm{eff}} = 3$) captured the dynamics well, whereas transitional regimes required higher degrees ($d_{\mathrm{eff}} = 5$–6), curvature, and Lipschitz values. These quantities thus serve as quantitative measures of cratering and its transitions, validating the use of a polynomial model.

The single-parameter coefficient models were developed and evaluated to assess how accurately the crater volume evolution can be predicted from limited operating conditions along each parameter slice. For variations in ambient pressure at a fixed mass flow rate and nozzle height, linear coefficient interpolation produces relative L_2 errors on the order of 0.3–0.5, with the largest errors occurring when extrapolating to the lowest and highest pressures, indicating insufficient accuracy with only three pressure cases. For variations in nozzle height at fixed mass flow rate and ambient pressure, prediction accuracy is highest at intermediate heights but degrades sharply at lower heights, with relative L_2 errors increasing from approximately 0.045 at $\bar{h}/\bar{d}_\mathrm{e} = 10$ to 0.54–0.73 at $\bar{h}/\bar{d}_\mathrm{e} = 5$–$6$, coinciding with annular–parabolic transition regimes. For variations in mass flow rate at fixed ambient pressure and nozzle height, the coefficient mapping collapses to a constant under leave-one-out validation, resulting in large errors (relative $L_2 \gtrsim 0.9$) due to the availability of only two mass-flow cases, demonstrating that sparse sampling and regime transitions limit the reliability of single-parameter inference.

Although the proposed framework is general and robust, its predictive capability remains limited by the number and distribution of available operating conditions, particularly in transition regimes where crater geometry changes. The current model does not account for soil properties in cratering. Future work can incorporate soil characteristics such as particle size and cohesion into the model. Future work should therefore focus not only on improving prediction, but also on advancing the physical understanding of plume-surface interaction. In this regard, the following research directions are recommended:

- Expand the dataset across transition regimes through additional experiments and high-fidelity numerical simulations, with denser sampling in ambient pressure, nozzle height, and mass flow rate to better resolve the onset and progression of crater-shape transitions.
- Investigate plume structure over different crater geometries by examining how impingement pattern, recirculation, jet spreading, pressure loading, and shear stress vary over annular, parabolic, conical-parabolic, conical-annular, and conical-deep craters, and how these variations relate to crater morphology.
- Study the coupling between crater geometry and plume behavior by determining how the evolving crater modifies the local flow field, influences subsequent erosion and crater

growth, and how the initial surface or crater geometry affects early-stage crater development.

- Relate crater-shape transitions to the underlying erosion physics by identifying how different crater geometries correspond to dominant mechanisms, including viscous erosion, bearing-capacity failure, diffusion-driven shearing, or their interaction.
- Develop improved predictive frameworks by extending the present single-parameter framework to coupled multi-parameter models that account for plume conditions, ambient environment, soil response, and evolving crater geometry, thereby moving toward more physics-informed predictive models.

References

[1] A. M. Korzun, C. J. Eberhart, J. West, P. Liever, A. Weaver, J. Mantovani, A. Langton, B. Kemmerer, and A. Atkins, "Design of a subscale, inert gas test for plume-surface interactions in a reduced pressure environment," in *AIAA Scitech 2022 Forum*, 2022, p. 1808.

[2] C. J. Eberhart, J. West, and A. M. Korzun, "Overview of plume-surface interaction data from subscale inert gas testing at nasa msfc test stand 300 vacuum facilities," in *AIAA Scitech 2022 Forum*, 2022, p. 1811.

[3] J. S. Rubio, M. Gorman, M. X. Diaz-Lopez, and R. Ni, "Plume-surface interaction physics focused ground test 1: Setup and preliminary results," in *AIAA SCITECH 2022 Forum*, 2022, p. 1809.

[4] C. Immer, P. Metzger, P. E. Hintze, A. Nick, and R. Horan, "Apollo 12 lunar module exhaust plume impingement on lunar surveyor iii," *Icarus*, vol. 211, no. 2, pp. 1089–1102, 2011.

[5] SpaceRef. (2008, Dec.) Four out of six apollos. SpaceNews. Posted in Press Release; updated July 15, 2024. [Online]. Available: https://spacenews.com/four-out-of-six-apollos/

[6] C. Q. LaMarche and J. S. Curtis, "Cratering of a particle bed by a subsonic turbulent jet: Effect of particle shape, size and density," *Chemical Engineering Science*, vol. 138, pp. 432–445, 2015.

[7] M. Mehta, N. O. Renno, J. Marshall, M. R. Grover, A. Sengupta, N. A. Rusche, J. F. Kok, R. E. Arvidson, W. J. Markiewicz, M. T. Lemmon *et al.*, "Explosive erosion during the phoenix landing exposes subsurface water on mars," *Icarus*, vol. 211, no. 1, pp. 172–194, 2011.

[8] D. Stubbs *et al.*, "An experimental investigation of crater formation physics during plume-surface interactions using non-intrusive measurement techniques," 2024.

[9] P. T. Metzger, C. D. Immer, C. M. Donahue, B. T. Vu, R. C. Latta III, and M. Deyo-Svendsen, "Jet-induced cratering of a granular surface with application to lunar spaceports," *Journal of Aerospace Engineering*, vol. 22, no. 1, pp. 24–32, 2009.

[10] J. Alexander, W. Roberds, and R. Scott, "Soil erosion by landing rockets final report," Tech. Rep., 1966.

[11] R. F. Scott and H.-Y. KO, "Transient rocket-engine gas flow in soil." *Aiaa Journal*, vol. 6, no. 2, pp. 258–264, 1968.

[12] P. T. Metzger, R. C. Latta III, J. M. Schuler, and C. D. Immer, "Craters formed in granular beds by impinging jets of gas," in *AIP Conference Proceedings*, vol. 1145, no. 1. American Institute of Physics, 2009, pp. 767–770.

[13] P. T. Metzger, C. D. Immer, C. M. Donahue, B. T. Vu, R. C. Latta III, and M. Deyo-Svendsen, "Jet-induced cratering of a granular surface with application to lunar spaceports," *Journal of Aerospace Engineering*, vol. 22, no. 1, pp. 24–32, 2009.

[14] C. Q. LaMarche, J. S. Curtis, and P. T. Metzger, *Cratering of a Lunar Soil Simulant, JSC-1A, by a Turbulent Subsonic Jet*, pp. 36–44. [Online]. Available: https://ascelibrary.org/doi/abs/10.1061/9780784412190.005

[15] P. T. Metzger, "Erosion rate of lunar soil under a landing rocket, part 1: Identifying the rate-limiting physics," *Icarus*, vol. 417, p. 116136, 2024.

[16] C. M. Donahue, P. T. Metzger, and C. D. Immer, "Empirical scaling laws of rocket exhaust cratering," in *56th International Astronautical Congress*, no. KSC-2005-162, 2005.

[17] D. C. Stubbs, L. Silwal, B. S. Thurow, M. Hirabayashi, V. Raghav, and D. E. Scarborough, "Three-dimensional measurement of the crater formation during plume–surface interactions using stereo-photogrammetry," *AIAA Journal*, vol. 60, no. 3, pp. 1316–1331, 2022.

[18] M. T. Gorman, J. S. Rubio, M. X. Diaz-Lopez, W. A. Chambers, A. M. Korzun, J. Rabinovitch, and R. Ni, "Scaling laws of plume-induced granular cratering," *PNAS nexus*, vol. 2, no. 9, p. pgad300, 2023.

[19] L. Bruni, M. Patel, F. Evrard, J. Capecelatro, and L. Villafañe Roca, "Data-driven characterization of crater morphology during plume-surface interaction," in *AIAA SCITECH 2025 Forum*, 2025, p. 2568.

[20] B. Dotson, A. St John, R. Hall, D. Sapkota, D. Britt, and P. Metzger, "Understanding the effects of geotechnical properties on viscous erosion rate from plume surface interactions," *Planetary and Space Science*, vol. 261, p. 106117, 2025.

[21] P. Benner, S. Gugercin, and K. Willcox, "A survey of projection-based model reduction methods for parametric dynamical systems," *SIAM review*, vol. 57, no. 4, pp. 483–531, 2015.

[22] S. L. Brunton, J. L. Proctor, and J. N. Kutz, "Discovering governing equations from data by sparse identification of nonlinear dynamical systems," *Proceedings of the national academy of sciences*, vol. 113, no. 15, pp. 3932–3937, 2016.

[23] G. E. Box and N. R. Draper, *Response Surfaces, Mixtures, and Ridge Analyses*. John Wiley & Sons, 2007.

[24] NASA, "NASA TechPort," https://techport.nasa.gov/projects/116277, n.d., accessed: 2024-12-08.

[25] J. Jing, S. Liu, G. Wang, W. Zhang, and C. Sun, "Recent advances on image edge detection: A comprehensive review," *Neurocomputing*, vol. 503, pp. 259–271, 2022.

[26] N. Ravi, V. Gabeur, Y.-T. Hu, R. Hu, C. Ryali, T. Ma, H. Khedr, R. Rädle, C. Rolland, L. Gustafson *et al.*, "Sam 2: Segment anything in images and videos," *arXiv preprint arXiv:2408.00714*, 2024.

[27] J. Gu, Z. Wang, J. Kuen, L. Ma, A. Shahroudy, B. Shuai, T. Liu, X. Wang, G. Wang, J. Cai *et al.*, "Recent advances in convolutional neural networks," *Pattern recognition*, vol. 77, pp. 354–377, 2018.

[28] R. Yamashita, M. Nishio, R. K. G. Do, and K. Togashi, "Convolutional neural networks: an overview and application in radiology," *Insights into imaging*, vol. 9, pp. 611–629, 2018.

[29] S. Xie and Z. Tu, "Holistically-nested edge detection," in *Proceedings of the IEEE international conference on computer vision*, 2015, pp. 1395–1403.

[30] Y. Liu, M.-M. Cheng, X. Hu, K. Wang, and X. Bai, "Richer convolutional features for edge detection," in *Proceedings of the IEEE conference on computer vision and pattern recognition*, 2017, pp. 3000–3009.

[31] J. Long, E. Shelhamer, and T. Darrell, "Fully convolutional networks for semantic segmentation," in *Proceedings of the IEEE conference on computer vision and pattern recognition*, 2015, pp. 3431–3440.

[32] R. Sun, T. Lei, Q. Chen, Z. Wang, X. Du, W. Zhao, and A. K. Nandi, "Survey of image edge detection," *Frontiers in Signal Processing*, vol. 2, p. 826967, 2022.

[33] K. Simonyan, "Very deep convolutional networks for large-scale image recognition," *arXiv preprint arXiv:1409.1556*, 2014.

[34] O. Ronneberger, P. Fischer, and T. Brox, "U-net: Convolutional networks for biomedical image segmentation," in *Medical image computing and computer-assisted intervention–MICCAI 2015: 18th international conference, Munich, Germany, October 5-9, 2015, proceedings, part III 18*. Springer, 2015, pp. 234–241.

[35] F. Milletari, N. Navab, and S.-A. Ahmadi, "V-net: Fully convolutional neural networks for volumetric medical image segmentation," in *2016 fourth international conference on 3D vision (3DV)*. Ieee, 2016, pp. 565–571.

[36] D. P. Kingma, "Adam: A method for stochastic optimization," *arXiv preprint arXiv:1412.6980*, 2014.

[37] Y. LeCun, L. Bottou, Y. Bengio, and P. Haffner, "Gradient-based learning applied to document recognition," *Proceedings of the IEEE*, vol. 86, no. 11, pp. 2278–2324, 1998.

[38] A. Krizhevsky, I. Sutskever, and G. E. Hinton, "Imagenet classification with deep convolutional neural networks," *Advances in neural information processing systems*, vol. 25, 2012.

[39] O. K. Tyrrell, N. S. Rodrigues, A. M. Korzun, and P. M. Danehy, "Flow visualization of intrusive and non-intrusive configurations for lunar-and martian-relevant plume-surface interaction," in *AIAA SCITECH 2024 Forum*, 2024, p. 2499.

[40] *American National Standard Specification for Octave-Band and Fractional-Octave-Band Analog and Digital Filters*, ser. ANSI S1.11-2004, Melville, NY, 2009.

[41] A. V. Oppenheim and R. W. Schafer, *Introduction to Signal Processing*. Englewood Cliffs, NJ: Prentice Hall, 2010.

[42] G. I. Austin, I. Pe'er, and T. Korem, "Distributional bias compromises leave-one-out cross-validation," *Science Advances*, vol. 11, no. 48, p. eadx6976, 2025.

[43] W. E. Gilbraith, C. P. Celani, and K. S. Booksh, "Visualization of confusion matrices with network graphs," *Journal of Chemometrics*, vol. 37, no. 3, p. e3435, 2023.

Appendices

Appendix A

Table A.1: Overview of parameter values for different experimental runs used in this study.

Regolith Simulant	Run	$\bar{p}_{\mathrm{amb}}$ [torr]	$\bar{h}/\bar{d}_{\mathrm{e}}$	$\bar{\dot{m}}$ [g/s]
	R1	0.053	10	0.32
	R2	4.5	3	8.6
	R4	0.053	4	0.32
	R5	2.003	4	8.6
	R7	2.003	3	0.32
	R8	4.5	3	0.32
	R9	0.053	3	8.6
	R10	4.5	3	8.6
	R11	2.003	3	8.6
	R12	0.053	10	0.32
	R13	4.5	10	0.32
	R14	0.053	10	8.6
	R15	2.003	10	0.32
	R16	2.003	10	8.6

Regolith Simulant	Run	$\bar{p}_{\mathrm{amb}}$ [torr]	$\bar{h}/\bar{d}_{\mathrm{e}}$	$\bar{\dot{m}}$ [g/s]
MDS	R17	4.5	10	8.6
	R18	0.02	13	0.32
	R19	0.2	13	0.32
	R20	0.2	13	8.6
	R21	2.003	13	0.32
	R22	2.003	13	8.6
	R23	0.02	5	0.32
	R24	0.02	6	0.32
	R25	0.02	8	0.32
	R26	0.02	10	0.32
	R27	2.003	13	0.32
	R28	0.02	5	0.32
	R29	0.02	8	$2\times$ 0.32
	R30	0.02	8	$4\times$ 0.32
	R31	4.5	10	8.6
	R32	0.2	10	8.6
BP-1	R53	4.5	10	0.32
	R91	0.02	3	0.32
	R92	0.02	6	0.32
BDS	R93	0.02	8	0.32
	R94	4.5	3	0.32
	R95	4.5	10	0.32
	R96	4.5	10	8.6
	R105	0.02	3	0.32
	R106	0.02	6	0.32

Regolith Simulant	Run	$\bar{p}_{\mathrm{amb}}$ [torr]	$\bar{h}/\bar{d}_{\mathrm{e}}$	$\bar{\dot{m}}$ [g/s]
TDM	R107	0.02	8	0.32
	R108	4.5	3	0.32
	R109	4.5	10	0.32
	R110	4.5	10	8.6
	R123	0.02	3	0.32
	R124	0.02	6	0.32
IRR	R125	0.02	8	0.32
	R126	4.5	3	0.32
	R127	4.5	10	0.32
	R128	4.5	10	8.6
	R137	0.02	3	0.32
	R138	0.02	6	0.32
MGB	R139	0.02	8	0.32
	R140	4.5	3	0.32
	R141	4.5	10	0.32
	R142	4.5	10	8.6

Appendix B

Polynomial fits for min-max normalized crater volume ($\hat{V}(h/d_{\mathrm{e}}, p_{\mathrm{amb}}, \dot{m}) \in [0,1]$ and time ($t \in [-1,1]$) are given as

$$
\begin{aligned}
\hat{V}_{(3,0.00529,6005.54)}(t) &= -0.352\,t^5 + 0.051\,t^4 + 0.473\,t^3 - 0.210\,t^2 + 0.373\,t + 0.646, \\
\hat{V}_{(3,5.37312,5.91287)}(t) &= 0.245\,t^5 - 0.121\,t^4 - 0.486\,t^3 + 0.041\,t^2 + 0.746\,t + 0.574, \\
\hat{V}_{(3,0.19988,158.90836)}(t) &= -0.667\,t^7 + 0.587\,t^6 + 1.263\,t^5 - 0.931\,t^4 - 0.941\,t^3 + \\
&\quad 0.267\,t^2 + 0.834\,t + 0.588, \\
\hat{V}_{(3,12.07141,2.63188)}(t) &= 0.196\,t^5 + 0.033\,t^4 - 0.487\,t^3 - 0.057\,t^2 + 0.795\,t + 0.527, \\
\hat{V}_{(3,0.44906,70.73188)}(t) &= -0.091\,t^3 - 0.222\,t^2 + 0.588\,t + 0.708, \\
\hat{V}_{(4,0.19988,158.90836)}(t) &= -0.129\,t^3 - 0.099\,t^2 + 0.636\,t + 0.587, \\
\hat{V}_{(5,0.05365,592.17384)}(t) &= 0.259\,t^4 - 0.242\,t^3 - 0.437\,t^2 + 0.734\,t + 0.689, \\
\hat{V}_{(6,0.05365,592.17384)}(t) &= 0.144\,t^4 - 0.246\,t^3 - 0.265\,t^2 + 0.731\,t + 0.629, \\
\hat{V}_{(8,0.05365,592.17384)}(t) &= 0.096\,t^4 - 0.167\,t^3 - 0.273\,t^2 + 0.659\,t + 0.677, \\
\hat{V}_{(8,0.05365,1184.34768)}(t) &= 0.225\,t^4 - 0.127\,t^3 - 0.486\,t^2 + 0.628\,t + 0.768, \\
\hat{V}_{(8,0.05365,2368.69535)}(t) &= 0.100\,t^4 - 0.051\,t^3 - 0.356\,t^2 + 0.564\,t + 0.747, \\
\hat{V}_{(10,0.05365,592.17384)}(t) &= 0.205\,t^5 + 0.082\,t^4 - 0.503\,t^3 - 0.161\,t^2 + 0.804\,t + 0.583,
\end{aligned}
$$

$$\hat{V}_{(10,0.14217,223.46183)}(t) = 1.420\,t^8 - 1.326\,t^7 - 1.953\,t^6 + 2.384\,t^5 - 0.108\,t^4 - 0.914\,t^3 + 0.538\,t^2 + 0.354\,t + 0.612,$$

$$\hat{V}_{(10,5.37312,5.91287)}(t) = -0.313\,t^5 + 0.064\,t^4 + 0.435\,t^3 - 0.320\,t^2 + 0.368\,t + 0.747,$$

$$\hat{V}_{(10,0.19988,158.90836)}(t) = -0.076\,t^3 - 0.009\,t^2 + 0.574\,t + 0.524,$$

$$\hat{V}_{(10,12.07141,2.63188)}(t) = -0.065\,t^3 - 0.127\,t^2 + 0.571\,t + 0.619,$$

$$\hat{V}_{(10,0.44906,70.73188)}(t) = 0.569\,t^6 + 0.147\,t^5 - 1.059\,t^4 - 0.406\,t^3 + 0.581\,t^2 + 0.762\,t + 0.422,$$

$$\hat{V}_{(13,0.05365,592.17384)}(t) = -0.207\,t^3 + 0.012\,t^2 + 0.699\,t + 0.492,$$

$$\hat{V}_{(13,0.53651,59.21738)}(t) = 0.169\,t^4 - 0.088\,t^3 - 0.354\,t^2 + 0.604\,t + 0.684,$$

$$\hat{V}_{(13,5.37312,5.91287)}(t) = 0.188\,t^6 - 0.072\,t^5 - 0.502\,t^4 + 0.042\,t^3 + 0.312\,t^2 + 0.524\,t + 0.501,$$

$$\hat{V}_{(13,0.19988,158.90836)}(t) = 0.173\,t^4 - 0.241\,t^3 - 0.316\,t^2 + 0.744\,t + 0.640.$$

Single parameter coefficient model for individual operating conditions. Coefficient were fitted on normalized operating parameter, ($p_{amb}, h/d_e$ or $\dot{m}$)$\in [-1, 1]$.

Table B.1: Linear ambient pressure-dependent coefficients for the baseline crater-volume model Eq. 5.3.

k	$c_{k,0}$	$c_{k,1}$
0	30.6459	7.15×10^{1}
1	15.8455	1.61×10^{2}
2	-5.8409	-3.14×10^{0}
3	-3.9918	6.17×10^{1}
4	1.3136	-1.11×10^{2}
5	-0.0140	-2.90×10^{1}
6	0.9285	6.14×10^{1}

Table B.2: Quadratic nozzle height-dependent coefficients for the baseline crater-volume model (Eq. 5.4).

k	$c_{k,0}$	$c_{k,1}$	$c_{k,2}$
0	-80.4700	25.9165	-1.4438
1	-22.5198	8.3044	-0.4051
2	4.6747	-3.3627	0.2419
3	19.5467	-6.0900	0.3077
4	2.3310	1.4841	-0.1456
5	-11.9548	3.3275	-0.1719
6	-1.0463	-0.5250	0.0557

Table B.3: Linear mass-flow-rate dependent coefficients for the baseline volume model, $\hat{V}(t;\dot{m}) = \sum_{k=0}^{6}\big(c_{k,0} + c_{k,1}\dot{m}\big)t^k$.

k	$c_{k,0}$	$c_{k,1}$
0	27.5086	3.38×10^{-5}
1	16.1234	5.28×10^{-5}
2	-21.0162	4.37×10^{-5}
3	4.5491	-2.95×10^{-5}
4	21.7999	-7.80×10^{-5}
5	-2.0977	1.07×10^{-5}
6	-10.7105	4.18×10^{-5}